NASA/TP-2018-220077

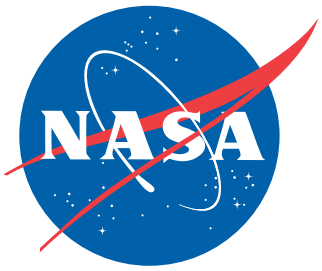

Light Ion Double-Differential Cross Sections for Space Radiation

John W. Norbury
Langley Research Center, Hampton, Virginia

July 2018

NASA STI Program . . . in Profile

Since its founding, NASA has been dedicated to the advancement of aeronautics and space science. The NASA scientific and technical information (STI) program plays a key part in helping NASA maintain this important role.

The NASA STI program operates under the auspices of the Agency Chief Information Officer. It collects, organizes, provides for archiving, and disseminates NASA's STI. The NASA STI program provides access to the NTRS Registered and its public interface, the NASA Technical Reports Server, thus providing one of the largest collections of aeronautical and space science STI in the world. Results are published in both non-NASA channels and by NASA in the NASA STI Report Series, which includes the following report types:

- TECHNICAL PUBLICATION. Reports of completed research or a major significant phase of research that present the results of NASA Programs and include extensive data or theoretical analysis. Includes compilations of significant scientific and technical data and information deemed to be of continuing reference value. NASA counter-part of peer-reviewed formal professional papers but has less stringent limitations on manuscript length and extent of graphic presentations.

- TECHNICAL MEMORANDUM. Scientific and technical findings that are preliminary or of specialized interest, e.g., quick release reports, working papers, and bibliographies that contain minimal annotation. Does not contain extensive analysis.

- CONTRACTOR REPORT. Scientific and technical findings by NASA-sponsored contractors and grantees.

- CONFERENCE PUBLICATION. Collected papers from scientific and technical conferences, symposia, seminars, or other meetings sponsored or co-sponsored by NASA.

- SPECIAL PUBLICATION. Scientific, technical, or historical information from NASA programs, projects, and missions, often concerned with subjects having substantial public interest.

- TECHNICAL TRANSLATION. English-language translations of foreign scientific and technical material pertinent to NASA's mission.

Specialized services also include organizing and publishing research results, distributing specialized research announcements and feeds, providing information desk and personal search support, and enabling data exchange services.

For more information about the NASA STI program, see the following:

- Access the NASA STI program home page at http://www.sti.nasa.gov

- E-mail your question to help@sti.nasa.gov

- Phone the NASA STI Information Desk at 757-864-9658

- Write to:
  NASA STI Information Desk
  Mail Stop 148
  NASA Langley Research Center
  Hampton, VA 23681-2199

NASA/TP-2018-220077

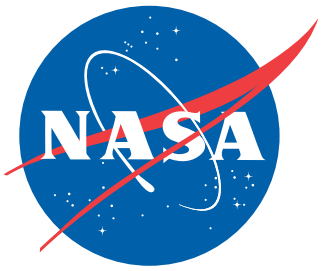

Light Ion Double-Differential Cross Sections for Space Radiation

John W. Norbury
Langley Research Center, Hampton, Virginia

National Aeronautics and
Space Administration

Langley Research Center
Hampton, Virginia 23681-2199

July 2018

Available from:

NASA STI Program / Mail Stop 148
NASA Langley Research Center
Hampton, VA 23681-2199
Fax: 757-864-6500

Acknowledgments

I wish to thank Drs. Charles Werneth, Tony Slaba, Ryan Norman, and Steve Smith for reviewing the manuscript. This work was supported by the Advanced Exploration Systems (AES) Division under the Human Exploration and Operations Mission Directorate of NASA.

Contents

List of Tables

List of Figures

Nomenclature

a	Constant used for calculation of the interaction radius R given in equation (29)
b	Constant used for calculation of the interaction radius R given in equation (29)
A	Mass number = total number of nucleons (neutrons, protons) in nucleus
$A_{\mathcal{P}}$	Mass number of projectile
$A_{\mathcal{T}}$	Mass number of target
$AAcm$	nucleus-nucleus center-of-momentum
β	Speed
c	Speed of light (units throughout paper are such that $c \equiv 1$)
c_A	Constant used for calculation of the coalescence coefficient C_A given in equation (28)
C_A	Coalescence coefficient calculated from equation (28)
cm	center-of-momentum
$\mathcal{C}$	Central fireball rest frame, or general symbol for central region
E	Total energy
γ	Relativistic factor $\gamma \equiv 1/\sqrt{1-\beta^2}$
L	Laboratory (lab) rest frame (identical to target rest frame, assuming stationary target)
m	Mass
$nncm$	nucleon-nucleon center-of-momentum
N	Normalization constant
Ω	Solid angle
j	Particle (fragment) index
p	Proton symbol
$\mathbf{p}$	3-momentum vector
p	Magnitude of 3-momentum vector $p \equiv \lvert\mathbf{p}\rvert$
$\mathcal{P}$	Projectile rest frame, or general symbol for projectile
ϕ	Azimuthal angle
R	Interaction radius
σ	Total cross section
$*$	Arbitrary rest frame (can be $\mathcal{C}, \mathcal{P}, \mathcal{T}$ or L)
T	Transverse component of a vector (e.g. transverse component of momentum is $\mathbf{p}_{\mathrm{T}}$)
T	Kinetic energy
$\mathcal{T}$	Target rest frame, or general symbol for target
θ	Longitudinal angle
Θ	Temperature
V	Interaction volume
X	Other fragments (in addition to the j particles of interest)
Z	Longitudinal component of a vector (e.g. longitudinal component of momentum is $\mathbf{p}_{\mathrm{Z}}$)

Nomenclature continued

$\frac{d\sigma}{dE}$	Energy single-differential cross section
$\frac{d\sigma}{d\Omega}$	Angle single-differential cross section
$\frac{d^2\sigma}{dEd\Omega}$	Non-invariant double-differential cross section
$E\frac{d^3\sigma}{dp^3}$	Lorentz-invariant double-differential cross section

Abstract

Neutrons and light ions have been shown to make large contributions to space radiation dose equivalent for realistic shielding scenarios. However, there are considerable uncertainties in the calculation of light ion production. Efficient and accurate calculation of light ion double-differential cross sections are required for input into space radiation transport codes. A thermal proton cross section model is developed which includes proton production from the 3 sources of projectile, central fireball, and target. It is shown that this 3-source model is able to explain the low-momentum, small-angle shoulder seen in proton spectra. Using the coalescence model, the thermal proton model is used to calculate light ion double-differential cross sections for use in space radiation transport codes. The 3-source model is also seen to be essential to explain the light ion shoulders, which are even more pronounced than the proton shoulders. Extensive comparisons between models and experimental measurements are shown and necessary future work is discussed.

1 Introduction

Light ions are defined to be isotopes of Hydrogen (H) and Helium (He); ions heavier than He are called heavy ions. Recent work [1, 2] has shown that neutrons and light ions provide the dominant contribution to space radiation dose equivalent for realistic spacecraft shielding of about 20 g/cm^2 or more. This is in contrast to thinly shielded regions of about 5 g/cm^2 or less, where the dominant contribution comes from high linear energy transfer (LET) heavy ions.

Given the importance of neutrons and light ions, there have been several studies that compare neutron and light ion production obtained by different transport techniques [3, 4]. The largest differences between various different transport codes occurs for light ion production. Furthermore, measurements of light ions on the Martian surface with the MSLRAD instrument show large differences between measurements and transport codes [5]. Therefore, *light ion production represents the largest physics uncertainty in space radiation studies.*

Neutrons and light ions are also special in that they scatter at large angles as they undergo transport within spacecraft shielding. High energy heavy ions, however, typically continue moving in the forward direction due to their large forward momentum. One-dimensional transport codes [6] employing the straight-ahead approximation have been used successfully to describe the transport of high energy heavy ions. However, this approximation fails for large angle scattering of neutrons and light ions, and special three-dimensional transport codes have been developed to calculate neutron and light ion transport through spacecraft [7, 8, 9, 10, 11].

Nuclear interaction cross sections are the fundamental input to transport codes. Cross sections are proportional to the probability of particle production in nuclear reactions. For example, an Iron (Fe) galactic cosmic ray (GCR) nucleus may strike an Aluminum (Al) spacecraft wall with the production of alpha (α) particles (i.e. ^{4}He nuclei). A cross section is proportional to the number of α particles produced. Total cross sections, σ (describing the total number of particles produced), and energy single-differential cross sections, $\frac{d\sigma}{dE}$ (describing the total number of particles produced at various energies E), are used in one-dimensional transport of heavy ions. However, due to the large angle scattering of neutrons and light ions, the type of cross section required is an energy-angle double-differential cross section, $\frac{d^2\sigma}{dEd\Omega}$ (describing the total number of particles produced at various energies E and at various angles Ω). Three-dimensional transport codes used for transporting neutrons and light ions require total cross sections, σ, single-differential cross sections, $\frac{d\sigma}{dE}$, and double-differential cross sections, $\frac{d^2\sigma}{dEd\Omega}$, as input.

Transport codes are typically either deterministic or stochastic, with the latter relying on Monte-Carlo (MC) techniques. NASA employs deterministic codes, such as HZETRN and 3DHZETRN, because they run much faster than MC codes and can therefore be utilized much more efficiently for spacecraft design and real-time evaluation of space radiation environments. These fast deterministic codes require the fast and efficient calculation of nuclear interaction cross sections. Cross sections can also be evaluated to a high degree of accuracy with MC techniques, but these are often too slow to be useful for deterministic transport and special fast parameterizations are often developed for cross section calculations [12].

The present work seeks to develop model calculations of double-differential cross section parameterizations for light ion production in high energy nuclear collisions of relevance to space radiation protection. The parameterizations are developed with the goal of fast and efficient cross section calculations that can be used in fast, deterministic three-dimensional transport codes. The models will then be compared to some of the available experimental data.

One might suppose that the large light ion discrepancies among transport codes, and between transport codes and MSLRAD measurements are due to the light ion cross section models used in the transport. The way to test this is to compare light ion cross section model calculations (such as those developed herein) to light ion cross section data measured at nuclear accelerators. A comprehensive study has been made of the available cross section data [13, 14, 15] that is relevant for space radiation. It was found that while there seems to be adequate data for heavy ions, the largest and most significant gaps were found for double-differential light ion cross sections, i.e. precisely those most needed for space radiation!

1.1 Light ion sources

In a high energy nucleus-nucleus collision the projectile and target nuclei collide and form a central fireball overlap region as shown in Figure 1, together with deformed and excited projectile and target pre-fragments, which decay into lighter fragments. This overall picture is often called the abrasion-ablation model [16]. The projectile and target fragments are often referred to as *spectator* fragments. The fireball region, often called the central or *participant* region, is generally very hot and contains excited baryons[1] and mesons.

The fireball decays quickly with the emission of pions, other mesons, and baryons such as neutrons, protons and other particles. The cooler excited projectile and target pre-fragments decay more slowly, generally by emitting nucleons, which may coalesce into light ions. In a high energy collision, the projectile pre-fragment is typically moving at the same speed as the original projectile. The target pre-fragment also moves, but an often-used approximation is to consider it stationary in the lab frame. There are therefore 3 different sources of particles, the projectile and target pre-fragments and the central fireball. Each of these 3 sources can produce the same type of particle that eventually reach particle detectors in the lab frame (or an astronaut's body in a spacecraft).

Many early works in theoretical heavy ion physics considered only contributions from either projectile fragmentation or central fireball emission. One of the first studies that considered adding contributions from both the projectile and central fireball was performed by Auble et al. [17]; however, target contributions were not taken into account. Up to now, for reactions with heavy ion projectiles, the set of HZETRN transport codes have included particles produced in the projectile frame only and have ignored any contributions from the central fireball and included only minor effects from the target.

1.2 Fireball physics

This sub-section examines issues that arise in determining the speed of the fireball; it will be shown that light ion cross section fireball contributions cannot continue to be ignored.

1.2.1 Fireball speed

Knowledge of the fireball's speed is essential to performing Lorentz-transformations of cross section model calculations from the fireball frame to the lab frame in which measurement data are listed. Relevant Lorentz-transformations are discussed in sections 3.1 and 7.

[1]The fundamental particles are called quarks and leptons from which all other non-dark particles in the universe are constructed. Electrons, muons and neutrinos are examples of leptons. Quarks join together in 2 quark (meson) and 3 quark (baryon) combinations. The lightest 3 quark combinations are the proton and neutron. The lightest 2 quark combination is called a pion, or pi (π) meson. There are several hundred known heavier baryons and mesons. Baryons and mesons are collectively called hadrons.

What is the central fireball speed? This would seem to be a question with a simple answer, yet there are a variety of possible approaches listed below:

- Nucleus-nucleus center-of-momentum (*AAcm*) frame: The simplest approach would be to use the *AAcm* frame as the fireball rest frame, with the speed of the fireball being identical to the speed of the *AAcm* frame.

- Nucleon-nucleon center-of-momentum (*nncm*) frame: In the thermal model developed by Nagamiya et al. [18], the kinetic energy of the emitted particle (proton or pion) is evaluated in the *nncm* frame; i.e., the speed of the central fireball is identical to the speed of the *nncm* frame. *The same approach is used in the present work.* The reactions studied in the present work are Ar + KCl and C + C. In these cases, the *nncm* frame is the same as the *AAcm* frame, because the projectile and target have equal mass numbers.

- Abrasion-ablation model: Using the abrasion-ablation model, one can determine the number of nucleons in the participant (fireball) region from a knowledge of the impact parameter. Therefore, the fireball speed becomes a function of impact parameter, which is averaged when calculating cross sections [19].

- Fitting to data: Auble et al. [17] developed a model involving both projectile and fireball contributions to cross sections, and performed a parameter optimization to obtain the best data fit. In this approach, the spectator and participant speeds were determined from the best fit to the data.

The approach used in the present work is to take the central fireball speed to be identical to the speed of the *nncm* rest frame, as in the study of Nagamiya et al. [18]. Future work (see section 5) will investigate alternative approaches.

1.2.2 Fireball contributions

HZETRN has always ignored contributions from the fireball. It will now be shown that this is not justified.

As shown in Figure 1, the projectile will continue to move forward at high speed after colliding with the target, while the target will remain close to rest. The speed of the fireball will be intermediate between these two. Questions that arise are:

1. Given that the fireball moves more slowly than the projectile, are fireball fragments sufficiently low in energy that they can be ignored?

2. Given that the fireball is very hot, do light ion fragments survive?

It will be shown below that the answers to both questions are negative, and that light ion contributions from the fireball cannot be ignored.

The relativistic expressions relating the total energy, E, kinetic energy, T, mass, m, and 3-momentum, $\mathbf{p}$, of the emitted fragment particle are the Einstein relations,

$$E \equiv T + m = \gamma m \ , \tag{1}$$

and

$$E^2 \equiv \mathbf{p}^2 + m^2 \ , \tag{2}$$

with units where the speed of light $c \equiv 1$; this standard convention is used throughout this paper. In terms of speed, β, the relativistic γ factor is $\gamma \equiv (1-\beta^2)^{-\frac{1}{2}}$. The speed of the projectile relative to the lab is $\beta_{\mathcal{P}L}$ with $\gamma_{\mathcal{P}L} \equiv (1-\beta_{\mathcal{P}L}^2)^{-\frac{1}{2}}$, and the speed of the nucleon-nucleon center-of-momentum ($nncm$) frame is β_{nncmL} with $\gamma_{nncmL} \equiv (1-\beta_{nncmL}^2)^{-\frac{1}{2}}$. The gamma factors are related via [20]

$$\gamma_{\mathcal{P}L} = 2\gamma_{nncmL}^2 - 1 \ . \tag{3}$$

Table 1 presents the speeds and energies of the projectile and fireball for typical projectile kinetic energy, $T_{\mathcal{P}L}$, values seen in the space radiation GCR spectrum. It is assumed that the speed of the fireball is equal to the speed of the $nncm$ frame. It can be seen that the projectile and fireball speeds, $\beta_{\mathcal{P}L}$ and β_{nncmL}, respectively, are similar orders of magnitude, as are the projectile and fireball nucleon energies, $E_{\mathcal{P}L}$ and E_{nncmL}, respectively. Since the speed and nucleon energy of the fireball is similar to that of the projectile (less than a factor of 2 for all cases in Table 1), the contributions of the fireball should not be ignored. This conclusion will not change if the fireball speed is calculated with one of the alternative methods discussed previously in section 1.2.1.

Next, question 2 concerning fragment survival from a very hot fireball will be addressed. Because the fireball is very hot, light ion fragments cannot survive and will be broken up into baryons and mesons. However, what happens when the fireball cools? The answer is similar to what happened in the very early universe. After a rapid period of inflation, the universe started as a quark-gluon plasma, which then cooled and formed hadrons such as pions, kaons, other mesons, nucleons, deltas, and other baryons. After further cooling the baryons decayed to nucleons, which later *coalesced* into light ions H, He and some Li[2]. Then the density dropped too rapidly to form heavier ions; these were made much later in stellar interiors (C - Fe), and both supernovae and binary neutron star mergers (Ni - U)[3]. The elements Be, B and some Li were made in cosmic ray interactions

[2]Big bang nucleosynthesis theory overestimates the amount of Li by a factor of 3 - the so-called Lithium problem [21, 22, 23, 24, 25].

[3]Recently verified when gravitational wave detection identified a binary neutron star merger, and rapid neutron capture nucleosynthesis [26] was confirmed in the accompanying electromagnetic signal [27]. Neutron star mergers [28] are now thought to be the primary source for producing the heaviest elements, like gold and platinum, which require a neutron-rich plasma. Previously, it was thought that supernovae were the source.

[26]. As the universe cooled further, electrons and light ions coalesced into atoms. Further cooling produced more coalescence, and molecules, gas, stars, and eventually galaxies formed due to gravitational coalescence.

Aspects of the nuclear fireball cooling are similar to the early universe scenario. As the fireball cools and decays and emits neutrons and protons, these are cool enough to coalesce into the light ion isotopes of H and He (and also some Li). As with the early universe, the fireball density drops very rapidly, and nucleons are unable to coalesce to form heavier ions, which come from projectile and target pre-fragments. Of course, the projectile and target pre-fragments also emit nucleons (neutrons and protons) and these can also coalesce. Thus, light ions are produced from nucleon coalescence of all 3 sources; projectile, fireball and target. The relative contributions of these will be explored further in the model developed in the present work.

2 Coalescence model

The coalescence model used herein is based on the work of Nagamiya et al. [18]. The light ion Lorentz-invariant double-differential cross section $E_A\, d^3\sigma_A/dp_A^3$ is related to the proton Lorentz-invariant double-differential cross section $E_{\rm p}\, d^3\sigma_{\rm p}/dp_{\rm p}^3$ as

$$E_A \frac{d^3\sigma_A}{dp_A^3} = C_A \left(E_{\rm p} \frac{d^3\sigma_{\rm p}}{dp_{\rm p}^3} \right)^A , \qquad \text{with } \; p_A \equiv A p_{\rm p} \; \text{ and } \; E_A \equiv A E_{\rm p} \, , \tag{4}$$

where E and $p \equiv |\mathbf{p}|$ are the energy and 3-momentum magnitude of the emitted fragment, and $p^3 \equiv p^2 dp d\Omega \equiv |\mathbf{p}|^2 d|\mathbf{p}| d\Omega$, with solid angle $d\Omega \equiv \sin\theta d\theta d\phi$. See the list of symbols in the Nomenclature table. A is the mass number of the light ion fragment and the p and A subscripts refer to a proton or light ion respectively. C_A is the coalescence model coefficient. The cross sections in equation (4) refer to light ion and proton fragment production for arbitrary projectile and target. For example, if the reaction being considered is Fe (1 GeV/n) + Al, the ^{3}He production cross section on the left hand side of equation (4) refers to Fe (1 GeV/n) + Al $\rightarrow$ ^{3}He +X, (where X are other produced fragments), with the proton (p) production cross section on the right hand side of equation (4) referring to Fe (1 GeV/n) + Al $\rightarrow$ p + X.

Note that in equation (4) the units of the light ion energy and momentum are GeV, not GeV/n. This is an essential feature when using the proton cross sections on the right hand side of equation (4) as input. The coalescence model gives the energy and momentum of the light ion as $p_A \equiv A p_{\rm p}$ and $E_A \equiv A E_{\rm p}$ respectively. (However, if a transport code requires GeV/n, the conversion is trivial.)

2.1 Coalescence scaling validation

The coalescence model scaling of equation (4) can be tested experimentally. This is done by scaling experimental proton data using equation (4), and then comparing the scaled data to experimental light ion data. There are no theoretical calculations anywhere in the process. Proton data is used as input on the right hand side of equation (4) and the left hand side becomes scaled proton data, which is compared to light ion data. Figures 2 - 8 show the results of these comparisons, where Figures 2 - 5 show the reaction Ar + KCl at 800 MeV/n projectile kinetic energy and Figures 6 - 8 show C + C at 800 MeV/n projectile kinetic energy. Note that the energy and momentum units used in all Figures 2 - 8 are GeV, and not GeV/n.

In Figures 2 - 8, the proton data from references [18, 29] is plotted in blue color, while light ion data is plotted in black color. Clearly these two data sets look as though they are completely un-related. The coalescence model is tested as follows: The proton data is inserted into the right hand side of equation (4), to arrive at the left hand side representing scaled proton data, represented in red color in Figures 2 - 8. *One can see the remarkable results of the coalescence idea; the scaled proton data (red) lies directly on top of the experimental light ion data (black).* This was first shown by Nagamiya et al. [18], where plots for the C + C reaction were shown in Figure 31 of reference [18].

The remarkable results shown in Figures 2 - 8 give strong support to the coalescence model. The aim of the present work is to *calculate* light ion cross sections for input into transport codes. Therefore, if one has an accurate theoretical model calculation of the proton cross sections, then using equation (4), one can scale these and immediately obtain accurate theoretical calculations of the light ion spectra. Figures 2 - 8 convincingly demonstrate that if a theoretical proton model accurately describes the proton data, then the theoretical light ion coalescence model using equation (4) will *automatically* describe the light ion data reasonably well.

Some of the experimental data for the Ar + KCl reactions have the same fragments at the same angles compared to the C + C reactions. Such data [18] are shown in Figure 9, with both data sets showing similar shapes and the C + C data always significantly lower than the Ar + KCl data.

3 Thermal particle production model

The general form of the thermal model [18] for emitting a particle fragment is now discussed. The emitted particle, for example, could be a pion, proton, neutron, light ion, or any other type of fragment.

The thermal model expression for the Lorentz-invariant double-differential cross sec-

tion for production of a fragment particle is

$$E\frac{d^3\sigma}{dp^3} = N\, e^{-T/\Theta}\ , \tag{5}$$

where T is the kinetic energy of the emitted fragment. The temperature Θ is given in units of energy and N is a constant. Equation (5) seems very simple, but its practical implementation is much more complicated, as seen later in equation (12).

3.1 Relativistic Lorentz-transformations

The cross section measured in the lab frame will contain contributions from the projectile, the fireball and the target. Note that the target is approximately at rest in the lab frame. Therefore the target rest frame is considered identical to the lab rest frame. Cross sections from each of these 3 frames must be Lorentz-transformed to the lab frame and added together to form the final lab frame cross section. The lab frame is also identical with the spacecraft rest frame through which GCR particles are transported. In any particle production cross section model, including thermal models, there will be contributions from all 3 sources.

Typically one might use the symbols $\mathcal{P}$, $\mathcal{C}$ or $\mathcal{T}$ for the projectile, central fireball or target rest frames respectively. However, the general expressions for the Lorentz-transformations will be the same for any frame and so a more compact notation using the $*$ symbol will be used, where $*$ refers to any of the projectile, central fireball or target rest frames. The symbols $\mathcal{P}$, $\mathcal{C}$ or $\mathcal{T}$ will only be used if it is necessary to specify a particular frame.

3.1.1 Total 3-momentum and angle variables (p_{jL}, θ_{jL})

Equation (5) is the general expression for a thermal model cross section evaluated in any of the 3 source frames discussed previously. The thermal model for a particle j emitted in the $*$ frame ($*$ = projectile or central fireball or target) is

$$\left[E\frac{d^3\sigma}{dp^3}(p_{jL}, \theta_{jL})\right]_* = N\, e^{-T_{j*}/\Theta_*} = N\, \exp[-T_{j*}(p_{jL}, \theta_{jL})/\Theta_*]\ , \tag{6}$$

where p_{jL} and θ_{jL} are the momentum and angle of particle j in the lab frame, L. The notation (p_{jL}, θ_{jL}) indicates that the functions must be written as explicit functions of the lab frame L variables p_{jL} and θ_{jL} because these are the variables used for the experimental cross sections, with which the thermal model is to be compared. However, T_{j*} is the kinetic energy of particle j in the $*$ frame, and this needs to be Lorentz-transformed to the lab frame, L. The temperature of the $*$ frame is Θ_*, which does not need to be Lorentz-transformed because it is a Lorentz-scalar.

In order to Lorentz-transform the particle j kinetic energy, use equation (1) to write

$$T_{j*} = E_{j*} - m_{j*} \ . \tag{7}$$

The Lorentz-transformation of the total energy is [30]

$$E_{j*} = \gamma_{*L} \ E_{jL} - \gamma_{*L} \ \beta_{*L} \ p_{ZjL} \ , \tag{8}$$

where the longitudinal momentum is given as $p_{ZjL} \equiv p_{jL} \cos\theta_{jL}$ with $p_{jL} \equiv |\mathbf{p}_{jL}|$. The relativistic γ_{*L} and β_{*L} factors refer to the speed of the $*$ frame with respect to the lab frame, L. That is, they are relations *between* different reference frames and have nothing to do with particle j. Thus, the Lorentz-transformed total energy of particle j in terms of (p_{jL}, θ_{jL}) variables is

$$E_{j*} = \gamma_{*L} \sqrt{p_{jL}^2 + m^2} - \gamma_{*L} \ \beta_{*L} \ p_{jL} \cos\theta_{jL} \ , \tag{9}$$

which is simply substituted into equation (6) via equation (7) to give the final answer for the thermal model Lorentz-invariant double-differential cross section in the $*$ frame,

$$\left[E \frac{d^3\sigma}{dp^3}(p_{jL}, \theta_{jL}) \right]_* = N \ \exp[-(\gamma_{*L} \sqrt{p_{jL}^2 + m^2} - \gamma_{*L} \ \beta_{*L} \ p_{jL} \cos\theta_{jL} - m_{jL})/\Theta_*] \ . \tag{10}$$

Once one has the right hand side of the Lorentz-invariant differential cross section of equation (6) written explicitly in terms of the lab, L, variables (p_{jL}, θ_{jL}), then one has the final answer as equation (10), which is the $*$ frame Lorentz-invariant differential cross section in terms of particle j lab frame variables (p_{jL}, θ_{jL}). The left hand side of equation (6) or (10) in terms of (p_{jL}, θ_{jL}) variables is the $*$ frame Lorentz-invariant differential cross section, which is equal to the lab frame Lorentz-invariant differential cross section precisely because the quantity $E\frac{d^3\sigma}{dp^3}$ is a *Lorentz-invariant* differential cross section.

Cross sections for j particles from the 3 sources need to be added together as

$$\begin{aligned} E \frac{d^3\sigma}{dp^3}(p_{jL}, \theta_{jL}) &= \left[E \frac{d^3\sigma}{dp^3}(p_{jL}, \theta_{jL}) \right]_{\mathcal{P}} + \left[E \frac{d^3\sigma}{dp^3}(p_{jL}, \theta_{jL}) \right]_{\mathcal{C}} + \left[E \frac{d^3\sigma}{dp^3}(p_{jL}, \theta_{jL}) \right]_{\mathcal{T}} \\ &= N \left(e^{-T_{jL}/\Theta_{\mathcal{P}}} + e^{-T_{jL}/\Theta_{\mathcal{C}}} + e^{-T_{jL}/\Theta_{\mathcal{T}}} \right) , \end{aligned} \tag{11}$$

which is the final model result to be compared to experiment. *The cross sections can be added in this simple way because they are all Lorentz-invariant.* Each of the 3 terms in equation (11) is calculated using equation (10), where $*$ is replaced by $\mathcal{P}$, $\mathcal{C}$ or $\mathcal{T}$ symbols representing projectile, central fireball or target, respectively. (Of course, the target frame is identical to the lab frame, so that the Lorentz-transformation is trivial, in that $\gamma_{\mathcal{T}L} = 1$ and $\beta_{\mathcal{T}L} = 0$, resulting in the identity $E_{j\mathcal{T}} = E_{jL}$.) Explicitly, equations (10) and (11)

give

$$E\frac{d^3\sigma}{dp^3}(p_{jL},\theta_{jL}) = N\{\exp[-(\gamma_{\mathcal{P}L}\sqrt{p_{jL}^2+m^2}-\gamma_{\mathcal{P}L}\,\beta_{\mathcal{P}L}\,p_{jL}\cos\theta_{jL}-m_{jL})/\Theta_{\mathcal{P}}] + \exp[-(\gamma_{\mathcal{C}L}\sqrt{p_{jL}^2+m^2}-\gamma_{\mathcal{C}L}\,\beta_{\mathcal{C}L}\,p_{jL}\cos\theta_{jL}-m_{jL})/\Theta_{\mathcal{C}}] + \exp[-(\gamma_{\mathcal{T}L}\sqrt{p_{jL}^2+m^2}-\gamma_{\mathcal{T}L}\,\beta_{\mathcal{T}L}\,p_{jL}\cos\theta_{jL}-m_{jL})/\Theta_{\mathcal{T}}]\}. \quad (12)$$

This equation represents the thermal model with contributions from the projectile, target and central sources, all Lorentz-transformed to the lab frame; equation (12) is the practical implementation of the simple-looking form of the thermal model in equation (5).

3.1.2 Transverse and longitudinal momentum variables $(p_{\mathrm{T}jL}, p_{\mathrm{Z}jL})$

Cross sections are also often measured in terms of transverse and longitudinal momentum variables, in which case equation (9) is replaced by

$$E_{j*} = \gamma_{*L}\sqrt{p_{\mathrm{T}jL}^2+p_{\mathrm{Z}jL}^2+m^2}-\gamma_{*L}\,\beta_{*L}\,p_{\mathrm{Z}jL}\ , \quad (13)$$

giving the final answer

$$\left[E\frac{d^3\sigma}{dp^3}(p_{\mathrm{T}jL},p_{\mathrm{Z}jL})\right]_* = N\exp[-(\gamma_{*L}\sqrt{p_{\mathrm{T}jL}^2+p_{\mathrm{Z}jL}^2+m^2}-\gamma_{*L}\,\beta_{*L}\,p_{\mathrm{Z}jL}-m_{jL})/\Theta_*]. \quad (14)$$

Equation (12) becomes

$$E\frac{d^3\sigma}{dp^3}(p_{\mathrm{T}jL},p_{\mathrm{Z}jL}) = N\{\exp[-(\gamma_{\mathcal{P}L}\sqrt{p_{\mathrm{T}jL}^2+p_{\mathrm{Z}jL}^2+m^2}-\gamma_{\mathcal{P}L}\,\beta_{\mathcal{P}L}\,p_{\mathrm{Z}jL}-m_{jL})/\Theta_{\mathcal{P}}] + \exp[-(\gamma_{\mathcal{C}L}\sqrt{p_{\mathrm{T}jL}^2+p_{\mathrm{Z}jL}^2+m^2}-\gamma_{\mathcal{C}L}\,\beta_{\mathcal{C}L}\,p_{\mathrm{Z}jL}-m_{jL})/\Theta_{\mathcal{C}}] + \exp[-(\gamma_{\mathcal{T}L}\sqrt{p_{\mathrm{T}jL}^2+p_{\mathrm{Z}jL}^2+m^2}-\gamma_{\mathcal{T}L}\,\beta_{\mathcal{T}L}\,p_{\mathrm{Z}jL}-m_{jL})/\Theta_{\mathcal{T}}]\}. \quad (15)$$

This equation replaces equation (12) if transverse and longitudinal momentum variables $(p_{\mathrm{T}jL}, p_{\mathrm{Z}jL})$ are used instead of the total 3-momentum and angle variables (p_{jL}, θ_{jL}) of the previous sub-section.

3.2 Normalization

3.2.1 Single-source model normalization

The total cross section, σ, is defined simply as the integral of the Lorentz-invariant differential cross section,

$$\sigma \equiv \int \frac{d^3p}{E}\left(E\frac{d^3\sigma}{dp^3}\right) = 4\pi\int_0^\infty dp\frac{p^2}{E}\left(E\frac{d^3\sigma}{dp^3}\right) = 4\pi\int_0^\infty dT\sqrt{T(T+2m)}\left(E\frac{d^3\sigma}{dp^3}\right) \ , \quad (16)$$

with the 4π factor arising from the assumption of isotropic emission of particles in the reference frame in which they are produced. Inserting the thermal model of equation (5) gives

$$\sigma = 4\pi N\int_0^\infty dT\sqrt{T(T+2m)}\ e^{-T/\Theta} \ . \quad (17)$$

Using the result

$$\int_0^\infty dT\sqrt{T(T+2m)}\ e^{-T/\Theta} = m\Theta e^{m/\Theta}K_1(m/\Theta) \ , \quad (18)$$

where $K_1(m/\Theta)$ is the modified Bessel function of the second kind [31] of order 1 as a function of m/Θ, giving the thermal model total cross section as

$$\sigma = 4\pi N m\Theta e^{m/\Theta}K_1(m/\Theta). \quad (19)$$

Substituting into equation (5), gives the single-source thermal model (correctly normalized so that the integral of the Lorentz-invariant differential cross section gives the total cross section), which therefore becomes

$$E\frac{d^3\sigma}{dp^3} = \frac{\sigma}{4\pi m\Theta K_1(m/\Theta)}\ e^{-(T+m)/\Theta} \ . \quad (20)$$

3.2.2 3-source model normalization

For the 3-source thermal model, the normalization is more complicated. The total cross section is obtained by integrating all 3 sources. Using equation (11) and following equation (16) gives

$$\begin{aligned}
\sigma &\equiv \int \frac{d^3p}{E}\left(E\frac{d^3\sigma}{dp^3}\right) \\
&= \int \frac{d^3p}{E}\left\{\left[E\frac{d^3\sigma}{dp^3}(p_{jL},\theta_{jL})\right]_{\mathcal{P}} + \left[E\frac{d^3\sigma}{dp^3}(p_{jL},\theta_{jL})\right]_{\mathcal{C}} + \left[E\frac{d^3\sigma}{dp^3}(p_{jL},\theta_{jL})\right]_{\mathcal{T}}\right\} \\
&= 4\pi\int_0^\infty dp\frac{p^2}{E}\left\{\left[E\frac{d^3\sigma}{dp^3}(p_{jL},\theta_{jL})\right]_{\mathcal{P}} + \left[E\frac{d^3\sigma}{dp^3}(p_{jL},\theta_{jL})\right]_{\mathcal{C}} + \left[E\frac{d^3\sigma}{dp^3}(p_{jL},\theta_{jL})\right]_{\mathcal{T}}\right\} \ ,
\end{aligned} \quad (21)$$

so that

$$\begin{aligned}
\sigma &= 4\pi \int_0^\infty dT \sqrt{T(T+2m)} \\
&\quad \times \left\{ \left[E\frac{d^3\sigma}{dp^3}(p_{jL},\theta_{jL}) \right]_{\mathcal{P}} + \left[E\frac{d^3\sigma}{dp^3}(p_{jL},\theta_{jL}) \right]_{\mathcal{C}} + \left[E\frac{d^3\sigma}{dp^3}(p_{jL},\theta_{jL}) \right]_{\mathcal{T}} \right\} \\
&= 4\pi N \int_0^\infty dT_{jL} \sqrt{T_{jL}(T_{jL}+2m)}\, (e^{-T_{jL}/\Theta_{\mathcal{P}}} + e^{-T_{jL}/\Theta_{\mathcal{C}}} + e^{-T_{jL}/\Theta_{\mathcal{T}}}) \\
&= 4\pi N m \left[\Theta_{\mathcal{P}} e^{m/\Theta_{\mathcal{P}}} K_1(m/\Theta_{\mathcal{P}}) + \Theta_{\mathcal{C}} e^{m/\Theta_{\mathcal{C}}} K_1(m/\Theta_{\mathcal{C}}) + \Theta_{\mathcal{T}} e^{m/\Theta_{\mathcal{T}}} K_1(m/\Theta_{\mathcal{T}}) \right] ,
\end{aligned} \tag{22}$$

giving the normalization

$$N = \frac{\sigma}{4\pi m \left[\Theta_{\mathcal{P}} e^{m/\Theta_{\mathcal{P}}} K_1(m/\Theta_{\mathcal{P}}) + \Theta_{\mathcal{C}} e^{m/\Theta_{\mathcal{C}}} K_1(m/\Theta_{\mathcal{C}}) + \Theta_{\mathcal{T}} e^{m/\Theta_{\mathcal{T}}} K_1(m/\Theta_{\mathcal{T}}) \right]} . \tag{23}$$

The full 3-source thermal model, correctly normalized so that the integral of the Lorentz-invariant differential cross section gives the total cross section, therefore becomes

$$\begin{aligned}
E\frac{d^3\sigma}{dp^3}(p_{jL},\theta_{jL}) &= \left[E\frac{d^3\sigma}{dp^3}(p_{jL},\theta_{jL}) \right]_{\mathcal{P}} + \left[E\frac{d^3\sigma}{dp^3}(p_{jL},\theta_{jL}) \right]_{\mathcal{C}} + \left[E\frac{d^3\sigma}{dp^3}(p_{jL},\theta_{jL}) \right]_{\mathcal{T}} \\
&= \frac{\sigma(e^{-T_{jL}/\Theta_{\mathcal{P}}} + e^{-T_{jL}/\Theta_{\mathcal{C}}} + e^{-T_{jL}/\Theta_{\mathcal{T}}})}{4\pi m \left[\Theta_{\mathcal{P}} e^{m/\Theta_{\mathcal{P}}} K_1(m/\Theta_{\mathcal{P}}) + \Theta_{\mathcal{C}} e^{m/\Theta_{\mathcal{C}}} K_1(m/\Theta_{\mathcal{C}}) + \Theta_{\mathcal{T}} e^{m/\Theta_{\mathcal{T}}} K_1(m/\Theta_{\mathcal{T}}) \right]} .
\end{aligned} \tag{24}$$

In terms of total 3-momentum and angle variables (p_{jL}, θ_{jL}) the final thermal model is

$$\begin{aligned}
E\frac{d^3\sigma}{dp^3}(p_{jL},\theta_{jL}) &= \frac{\sigma}{4\pi m} \{ \exp[-(\gamma_{\mathcal{P}L}\sqrt{p_{jL}^2+m^2} - \gamma_{\mathcal{P}L}\,\beta_{\mathcal{P}L}\,p_{jL}\cos\theta_{jL} - m_{jL})/\Theta_{\mathcal{P}}] \\
&\quad + \exp[-(\gamma_{\mathcal{C}L}\sqrt{p_{jL}^2+m^2} - \gamma_{\mathcal{C}L}\,\beta_{\mathcal{C}L}\,p_{jL}\cos\theta_{jL} - m_{jL})/\Theta_{\mathcal{C}}] \\
&\quad + \exp[-(\gamma_{\mathcal{T}L}\sqrt{p_{jL}^2+m^2} - \gamma_{\mathcal{T}L}\,\beta_{\mathcal{T}L}\,p_{jL}\cos\theta_{jL} - m_{jL})/\Theta_{\mathcal{T}}] \} \\
&\quad \times \left\{ \Theta_{\mathcal{P}} e^{m/\Theta_{\mathcal{P}}} K_1(m/\Theta_{\mathcal{P}}) + \Theta_{\mathcal{C}} e^{m/\Theta_{\mathcal{C}}} K_1(m/\Theta_{\mathcal{C}}) + \Theta_{\mathcal{T}} e^{m/\Theta_{\mathcal{T}}} K_1(m/\Theta_{\mathcal{T}}) \right\}^{-1} .
\end{aligned} \tag{25}$$

In terms of transverse and longitudinal momentum $(p_{\mathrm{T}jL}, p_{\mathrm{Z}jL})$ the final thermal model is

$$E\frac{d^3\sigma}{dp^3}(p_{\mathrm{T}jL}, p_{\mathrm{Z}jL}) = \frac{\sigma}{4\pi m}\{\exp[-(\gamma_{\mathcal{P}L}\sqrt{p_{\mathrm{T}jL}^2 + p_{\mathrm{Z}jL}^2 + m^2} - \gamma_{\mathcal{P}L}\,\beta_{\mathcal{P}L}\,p_{\mathrm{Z}jL} - m_{jL})/\Theta_{\mathcal{P}}]$$
$$+\exp[-(\gamma_{\mathcal{C}L}\sqrt{p_{\mathrm{T}jL}^2 + p_{\mathrm{Z}jL}^2 + m^2} - \gamma_{\mathcal{C}L}\,\beta_{\mathcal{C}L}\,p_{\mathrm{Z}jL} - m_{jL})/\Theta_{\mathcal{C}}]$$
$$+\exp[-(\gamma_{\mathcal{T}L}\sqrt{p_{\mathrm{T}jL}^2 + p_{\mathrm{Z}jL}^2 + m^2} - \gamma_{\mathcal{T}L}\,\beta_{\mathcal{T}L}\,p_{\mathrm{Z}jL} - m_{jL})/\Theta_{\mathcal{T}}]\}$$
$$\times\left\{\Theta_{\mathcal{P}}e^{m/\Theta_{\mathcal{P}}}K_1(m/\Theta_{\mathcal{P}}) + \Theta_{\mathcal{C}}e^{m/\Theta_{\mathcal{C}}}K_1(m/\Theta_{\mathcal{C}}) + \Theta_{\mathcal{T}}e^{m/\Theta_{\mathcal{T}}}K_1(m/\Theta_{\mathcal{T}})\right\}^{-1}. \quad (26)$$

3.3 Thermal proton production model

The coalescence model gives light ion production cross sections in terms of proton production cross sections, as given by equation (4). Therefore, the key to the success of the coalescence model is the ability to accurately calculate the proton production cross section. Equations (5, 20) are general thermal model descriptions for production of any type of fragment from a single source. Previous sub-sections have described how to practically implement this model when the fragments are being produced from the 3 different sources of projectile, fireball or target, as given by equations (24, 25, 26). Now the general thermal model will be implemented specifically for production of proton fragments.

3.3.1 Total cross section values

Equations (20, 24, 25, 26) give the Lorentz-invariant double differential cross section for fragment production, with normalization such that the integral of the differential cross section gives the total cross section, σ. Therefore, a separate model is needed to calculate σ. The present work uses the NUCFRG3 [12] model, but any other type of model could be used. Calculations for proton strong interaction production cross sections from nucleus-nucleus reactions are listed in Table 2. For the Ar +KCl and C+C reactions, the contributions from electromagnetic dissociation interactions are small [32, 33] and are not included in the present work.

3.3.2 Adjustable temperature parameters

The entire set of models developed in the present work use only two adjustable parameters, which are the participant (central fireball) and spectator (projectile or target) temperatures. These are summarized in Table 3.

As mentioned previously, the nucleus-nucleus reaction contains two spectator pre-fragments, namely the projectile and target, as well as a participant region which is the central fireball, as seen in Figure 1. From the center-of-momentum frame it makes

sense for both spectators to have the same temperature, given that temperature is a Lorentz-scalar. The participant region will be much hotter than the spectators. Values for these parameters are listed in Table 3. The choices were guided from values listed in the literature [18], and were based on best fits to the data. Note that the participant temperature is about 3 times higher than the spectator temperatures. Future work will involve using a detailed model for predicting these temperatures.

This work examines 47 different data sets, summarized in Table 4. The complete number of data points is over 1,000. The proton production theory only has the two temperature parameters, and the light ion coalescence model has no parameters. The combined proton - thermal and light ion - coalescence models are able to approximately predict over 1,000 data points based on only these two temperature parameters.

3.4 Proton thermal model validation

The proton production thermal model Lorentz-invariant double-differential cross sections for Ar + KCl and C + C reactions are shown in Figures 10 and 11 respectively. Both reactions have projectile kinetic energy of 800 MeV/n. Figures 10 and 11 show total (red) and individual contributions from projectile (green), target (purple) and central fireball (blue). The figures show protons being produced at various angles in the lab frame. The total (red) result is the one that should be compared to the data.

The relative contributions of the projectile (green), target (purple) and central fireball (blue) are interesting to study as the proton production angle changes. Thermal model production of protons is assumed to be isotropic in the frame in which the protons are produced. While the projectile and central fireball proton contributions vary, the target contribution remains the same as the angle changes. This is expected because the lab frame in which the momentum and angle of the proton are measured is identical to the target frame, and no Lorentz-transformation is required, since the speed of the target frame with respect to the lab is $\beta_{TL} = 0$.

At small angles, Figures 10 and 11 show that the projectile protons contribute the most at large proton momenta, with the central fireball protons contributing most at intermediate momenta. This is because the projectile is moving much faster than the central fireball, even though the fireball is hotter. Nevertheless, because the fireball is so hot it also makes contributions at large momenta. At very small momenta the target contribution is large.

As the proton production angle increases, the projectile contribution becomes smaller because projectile protons are mainly boosted in the forward direction and only very high energy thermal protons can exit at larger angles; therefore, at the largest angles the projectile contribution is negligible. At intermediate angles, central fireball production of protons is dominant.

At the largest angles, only central fireball protons of very high energy can reach large angles in the lab frame, and so the central fireball protons contribute less, with target

protons contributing a large amount at large angles.

The contributions of protons from the projectile, target and central fireball give the total (red) production cross section in Figures 10 and 11 according to equations (11) and (12). These total results are to be compared to the experimental data. While pion production cross sections show a smooth exponential fall-off with increasing momenta [4, 34, 35], due to dominant production from the central fireball, the proton cross sections show a significantly different behavior at small angles. The dominant small angle feature is a flat region that can be seen at lower momenta. This is seen not only in the proton spectra (Figures 9 - 11), but also the light ion spectra (Figures 2 - 9). *This shoulder feature was the main reason for introducing the model of the present work to include projectile, fireball and target contributions.* For pion cross sections, only a central fireball thermal model is all that is necessary to fit the data [4, 34, 35], whereas the shoulder region in the proton and light ion data necessitated the development of the present 3-source model.

One of the main results of the present work is to show that the shoulder region of Figures 10 and 11 can be reproduced by summing projectile and fireball contributions. One of the first papers to develop this idea was by Auble et al. [17]. In summary, Figures 10 and 11 show that the proton spectral data can be reasonably reproduced with the 3-source thermal proton model developed herein.

4 Predicting light ion cross sections

The coalescence model of equation (4) is used to make predictions for light ion double-differential cross sections using the thermal model for the proton double-differential cross sections, as given by equations (12) or (15). That is, equations (12) or (15) are used as input to the right hand side of equation (4), by summing each source and then raising the entire sum to the power A. In terms of (p_{jL}, θ_{jL}) variables, this becomes[4]

$$E_A \frac{d^3\sigma_A}{dp_A^3} = C_A \left\{ \left[E\frac{d^3\sigma}{dp^3}(p_{jL},\theta_{jL}) \right]_{\mathcal{P}} + \left[E\frac{d^3\sigma}{dp^3}(p_{jL},\theta_{jL}) \right]_{\mathcal{C}} + \left[E\frac{d^3\sigma}{dp^3}(p_{jL},\theta_{jL}) \right]_{\mathcal{T}} \right\}^A , \quad (27)$$

which is the model used in the present work. Equation (27) is the correct form consistent with the coalescence model, and is physically motivated as follows: The coalescence scaling of the experimental proton data provided excellent agreement with the experimental light ion data. The scaled proton data relied simply on the overall proton cross sections - they were not broken into individual pieces. All sources contributed to the experimental proton cross sections. Therefore, equation (27) is consistent with the method of comparing the

[4]From a quantum mechanical point of view, the correct summing method is to add the quantum mechanical *amplitudes* instead of the classical approximation of adding cross sections. Adding quantum amplitudes will result in the model of equation (27) with additional interference terms appearing. The model in the present work uses the classical approximation.

scaled proton data with the light ion data. It is the overall scaled experimental proton cross section, rather than each individual source piece, that is used to obtain the excellent agreement with light ion experimental data. Also physically, equation (27) makes more sense because a single coalesced light ion could receive contributions from several sources. The model of equation (27) also produces better validation results compared to a model in which each source term is summed separately.[5]

4.1 Coalescence coefficient

Observed [18] and calculated coalescence coefficients, C_A, are shown in Table 5. The observed values are taken from Table VIII in the paper of Nagamiya et al. [18]. The calculations also follow the method outlined by Nagamiya et al. [18] and proceed as follows. The coalescence coefficient, C_A, is calculated as [18]

$$C_A = \frac{c_A}{V^{A-1}} \,, \tag{28}$$

where c_A is a constant for each value of A, i.e. it is a constant which changes only if the mass number A of the produced fragment changes. Equation (28) is actually the non-relativistic limit of the coefficient in reference [18]: This is sufficient due to the very weak energy dependence of C_A, as seen in Table VIII of reference [18]. The interaction volume is $V = \frac{4}{3}\pi R^3$, with the interaction radius R given by [18]

$$R = a(A_{\mathcal{P}}^{1/3} + A_{\mathcal{T}}^{1/3}) + b \,, \tag{29}$$

where a and b are constants from reference [18] listed in Table 6, and $A_{\mathcal{P}}$ and $A_{\mathcal{T}}$ are the mass numbers of the projectile and target nuclei, respectively.

The calculated C_A values in equation (28) require the constant c_A values as input. These c_A are constants, which vary only with A. That is, c_A takes three different values (see Table 7) depending on whether the fragment is ^{2}H, ^{3}H, ^{3}He, ^{4}He, with the value for ^{3}H and ^{3}He being the same because the A number ($A = 3$) is the same. The values of c_A are *not* discussed in reference [18], and therefore, in the present work, they have been determined from the reaction Ar (800MeV/n) + KCl as follows,

$$c_A = C_A^{\text{obs[Ar(800MeV/n)+KCl]}}\, V^{A-1} \,, \tag{30}$$

[5]Summing each term separately results in a model of the form

$$E_A \frac{d^3\sigma_A}{dp_A^3} = C_A \left\{ \left[E\frac{d^3\sigma}{dp^3}(p_{jL}, \theta_{jL}) \right]_{\mathcal{P}}^{A} + \left[E\frac{d^3\sigma}{dp^3}(p_{jL}, \theta_{jL}) \right]_{\mathcal{C}}^{A} + \left[E\frac{d^3\sigma}{dp^3}(p_{jL}, \theta_{jL}) \right]_{\mathcal{T}}^{A} \right\}.$$

This model was not used because it is not physically motivated and it was also found to give poorer validation results.

where $C_A^{\text{obs[Ar(800MeV/n)+KCl]}}$ are the observed C_A values (see Table 5) for the reaction of Ar (800MeV/n) + KCl [18]. The reason that a single reaction can be chosen to determine c_A is that c_A values are the same for all reactions producing the same fragment. The Ar (800MeV/n) + KCl reaction was chosen because it includes observed values for ^{4}He, which are missing for other reactions (see Table 5). Values[6] for c_A are listed in Table 7, showing that the only dependence is on the light ion fragment mass number A. Only the *three* values in Table 7 are used for calculation of the *entire* set of reactions in Table 5, and for *all other* light ion cross section predictions.

The calculated coalescence coefficients, C_A, and interaction radii, R, listed in Table Table 5 are seen to be in reasonable agreement with the observed values. Note that both of these calculated quantities are independent of projectile kinetic energy, as seen in Table 5. Also, they have the same value for the same mass number A, so that values for ^{3}H and ^{3}He are the same, as also seen in Table 5.

4.2 Light ion coalescence model validation

The light ion production coalescence model Lorentz-invariant double-differential cross sections for Ar + KCl and C + C reactions are shown in Figures 12 - 18. As with the proton cross sections, the light ion figures show total (red) and individual contributions from projectile (green), target (purple) and central fireball (blue), with the relative kinematic contributions of the 3 sources showing similar angular behavior to the proton cross sections, discussed in sub-section 3.4. *Similar conclusions regarding the relative contributions of projectile and central fireball as a function of angle were also discussed by Auble et al. [17]. See page 1556 of that reference.* At small angles, the low-momentum, small-angle shoulder region of the spectra is even more pronounced for light ions compared to protons, and the addition of the 3 sources is essential to explain the light ion shoulders. Overall, the light ion model provides a reasonable characterization of the experimental data.

5 Future work

The light ion model used in the present work consisted of the coalescence model which used proton production cross sections as input. Using only experimental data, it was shown that if one could obtain accurate proton cross sections then the coalescence model accurately predicts light ion cross sections. Therefore, it is important that the proton model provides an accurate description of experimental proton data. The most important future work is to obtain a larger data set and develop predictable theories to replace the adjustable parameters of Table 3. The following list of future work is in order of priority.

[6] As already stated, c_A depends on the A number of the fragment produced, whereas it is misleadingly written simply as c (independent of A) in the work of reference [18].

1. Develop a model that predicts projectile, target and fireball temperatures with the correct dependence on $A_{\mathcal{P}}$, $A_{\mathcal{T}}$ and projectile kinetic energy. Some useful references are [17, 18], where reference [18] shows a rather strong energy dependence.

2. Investigate a temperature model either relating temperature to nucleon-nucleon center of momentum kinetic energy or implementing the model of reference [45].

3. Develop a more accurate method for evaluating the central fireball speed.

4. Make *predictions* for light ion total cross sections, by integrating the Lorentz-invariant double differential cross sections developed in the present work.

5. Implement models into the 3DHZETRN space radiation transport code and update the code. The models developed in the present work have all been written using *Mathematica*. These need to be converted to *FORTRAN*.

6. Compare the updated 3DHZETRN code with measurements such as those obtained with MSLRAD [5, 36, 37].

7. Develop a high energy proton and light ion production model. The thermal models discussed in the present work are expected to be accurate in the intermediate energy region, but not at high energy. A high energy model, perhaps based on Feynman scaling, needs to be developed. Existing models [34, 38, 39] can be adapted.

8. Double-differential and single differential electromagnetic dissociation contributions [32, 33] need to be added to the models developed herein. Existing models [32] can be adapted.

9. Remove the non-relativistic limit approximation for the coalescence coefficient in equation (28).

10. Compare cross section models to a wider set of experimental data, especially for light ion projectiles. Some useful data are contained in references [18, 19, 29, 40, 41, 42, 43, 46, 47].

11. Some data [40] display peaks for proton production cross sections, whereas other data display a flat shoulder region; the latter data have been analyzed in the present work. Develop models to explain both types of data.

12. Compare cross section model predictions to other models, such as those used in the Russian (ROSCOSMOS) SHIELD transport code [3, 4] and other transport codes.

13. Investigate alternative models [17] to calculate coalescence coefficients. The aim would be to investigate models that promise higher accuracy.

14. Re-evaluate c_A values from equations (28) and (30) and Table 7 by averaging with the Ar + Pb reactions at the same energy. The Ar + Pb reaction listed in Table VIII of reference [18] is useful because it has values for α particles. Note that in principle, c_A only depends on the light ion fragment A, and should be the same for *all* reactions. This needs to be investigated. Values for c_A could potentially be obtained by averaging over all reactions listed in Table VIII of reference [18].

15. Investigate quantum mechanical corrections to the classical approximation used in equation (27).

16. Implement uncertainty quantification methods to quantify differences between model results and experimental data.

17. Make further recommendations for future cross section measurements.

6 Conclusions

Previous work [1, 2] has shown that neutrons and light ions provide the dominant contribution to space radiation dose equivalent for realistic spacecraft shielding of the order of 20 g/cm^2 or more. Because light ions are so important, one would think that the relevant physics needed for space radiation is well characterized. However, comparisons of light ion production among different transport codes and with experimental measurements show significant discrepancies. In fact, light ion production represents the largest physics uncertainty in space radiation studies. Luckily, the largest discrepancies are in energy regions that make only minor contributions to dose equivalent, and so model predictions of dose equivalent remain reasonably accurate. However, dose equivalent is not the only quantity of interest in space radiation studies, and it is prudent to try to resolve remaining physics and transport discrepancies.

Because of their relatively light mass compared to heavy fragment production, neutrons and light ions are scattered at large angles when produced from high energy cosmic ray interactions. Therefore, fully 3-dimensional transport methods [7, 8, 9, 10, 11] are required, and consequently, accurate double-differential cross section models are needed for input into 3-dimensional transport codes. Fast and efficient transport codes are used in space radiation studies and consequently efficient cross section parameterization models are desired.

A summary of the work presented in this paper follows:

- The coalescence formalism was tested using only experimental data and was found to be highly accurate in predicting light ion cross sections using proton cross sections as input. Consequently, one only needs to develop an accurate proton production cross section model. This can then be scaled using the coalescence model to provide accurate predictions of light ion cross sections.

- A thermal model for proton production was developed, with the important feature that all 3 sources of projectile, central fireball and target production of protons was included. This feature was able to explain the distinctive low-momentum, small-angle shoulder region in the proton spectrum.

- The 3-source proton thermal model was used as input into the coalescence model[7], to arrive at a cross section model for light ion production, which necessarily also includes 3 sources, which are seen to be essential in explaining the light ion shoulders, which are even more pronounced than the proton shoulders.

- The final cross section model developed herein represents a very fast parameterization of proton and light ion double-differential cross sections that can be used efficiently in space radiation transport codes.

- Validation has been performed at 3 different levels. 1) Coalescence scaling has been validated by showing that the coalescence-scaled proton data agrees with light ion data to a remarkable degree of precision. 2) The thermal proton model has been validated by comparing to 17 data sets. 3) The light ion coalescence model has been validated by comparing to 30 data sets. The total 47 data sets contain over 1,000 data points.

- Future work will focus on physics calculations of the temperature parameters and more extensive comparisons to experimental data.

7 Appendix: Relativistic γ factors

Using equation (1), the relativistic γ factor of the projectile frame relative to the lab frame is

$$\gamma_{\mathcal{P}L} = 1 + \frac{T_{\mathcal{P}L}}{m_n} \, , \tag{31}$$

where m_n is the nucleon mass and $T_{\mathcal{P}L}$ is the kinetic energy of the projectile relative to the lab in units of *energy per nucleon*. Note, that this is the only place where units of GeV/n are used. This is simply the kinetic energy of the projectile and serves *only* to give the values of the various γ factors. As stated perviously, everything else in the present

[7]Because of the coalescence scaling model developed in the present work, the entire theoretical development is in units of GeV, and not GeV/n. Also, the x-axis of all figures are plotted in units of GeV, because the original experimental data is in these units. One of the keys to the success of the overlapping plots in Figures 2 - 8 is the fact that the light ion cross sections are given in units of GeV, and not GeV/n. Of course if GeV/n was used, then the scaled proton data would not overlap the light ion data. Many transport codes use units of GeV/n, which of course is not a problem, because one simply makes the trivial conversion to GeV/n, not affecting the successful coalescence model in any way.

work is in units of GeV, not GeV/n; these GeV units refer to the energy and momentum of the produced light ion fragments.

The γ factor of the nucleus-nucleus center-of-momentum ($AAcm$) frame relative to the lab frame is [44]

$$\gamma_{AAcmL} = \frac{A_{\mathcal{P}}(T_{\mathcal{P}L} + m_n) + A_{\mathcal{T}} m_n}{\sqrt{m_n[m_n(A_{\mathcal{P}} + A_{\mathcal{T}})^2 + 2A_{\mathcal{P}}A_{\mathcal{T}}T_{\mathcal{P}L}]}} \; . \tag{32}$$

The γ factor of the nucleon-nucleon center-of-momentum ($nncm$) frame relative to the lab frame is obtained by setting $A_{\mathcal{P}} = A_{\mathcal{T}} = 1$ to give

$$\gamma_{nncmL} = \sqrt{1 + \frac{T_{\mathcal{P}L}}{2m_n}} \; , \tag{33}$$

yielding the relation between the $nncm$ and projectile γ factors as

$$\gamma_{\mathcal{P}L} = 2\gamma_{nncmL}^2 - 1 \; . \tag{34}$$

$T_{\mathcal{P}L}$ (MeV/n)	$\gamma_{\mathcal{P}L}$	$\beta_{\mathcal{P}L}$	$E_{\mathcal{P}L} = \gamma_{\mathcal{P}L} m_n$ (MeV)	γ_{nncmL}	β_{nncmL}	$E_{nncmL} = \gamma_{nncmL} m_n$ (MeV)
0	1	0	938	1	0	938
100	1.1	0.4	1038	1.0	0.22	962
500	1.5	0.8	1438	1.1	0.5	1056
1000	2.1	0.9	1938	1.2	0.6	1161
10,000	12	0.99	10,938	2.5	0.9	2360

Table 1: Projectile versus fireball kinematic quantities, assuming that the fireball moves at the same speed as the *nncm* frame. $X_{\mathcal{P}L}$ is the X value of the projectile ($\mathcal{P}$) frame relative to the lab frame (L), where X represents T, γ, β or E. X_{nncmL} is the X value of the *nncm* frame relative to the lab frame.

Reaction	σ (b)
Ar (800 MeV/n) + KCl $\rightarrow$ p + X	16
C (800 MeV/n) + C $\rightarrow$ p + X	3.5

Table 2: Total strong interaction cross sections calculated from NUCFRG3 [12].

Participant (Central Fireball) Temperature	$\Theta_{\mathcal{C}}$	110 MeV
Spectator (Projectile = Target) Temperature	$\Theta_{\mathcal{P}} = \Theta_{\mathcal{T}}$	35 MeV

Table 3: Adjustable temperature parameters.

Reactions	Fragments	Angles (degrees)
Ar (800 MeV/n) + KCl	Proton	10, 15, 20, 30, 40, 50, 60, 70, 80, 90, 100, 110, 145
	Deuteron	10, 30, 60, 80, 110, 145
	Triton	15, 30, 60, 80, 110, 145
	Helion	15, 30, 60, 80
	Alpha	15, 30, 60, 80
C (800 MeV/n) + C	Proton	15, 45, 70, 145
	Deuteron	15, 45, 70, 145
	Triton	15, 45, 70
	Helion	15, 45, 70

Table 4: Summary of 47 data sets studied. Each data set contains an average of 24 points, so that the total number of data points studied is over 1,000.

		^{2}H		^{3}H		^{3}He		^{4}He	
Kinetic Energy (MeV/n)	Reaction	C_A	R (fm)	C_A	R (fm)	C_A	R (fm)	C_A	R (fm)
400	Ne+NaF	1.4×10^{-5}	3.5	1.3×10^{-10}	3.1	8.0×10^{-11}	3.3		
		1.0×10^{-5}	3.3	0.6×10^{-10}	2.9	0.6×10^{-10}	2.9	9.3×10^{-16}	2.3
	Ne+Cu	8.0×10^{-6}	3.7	5.0×10^{-11}	3.2	3.0×10^{-11}	3.4		
		8.1×10^{-6}	3.6	3.6×10^{-11}	3.2	3.6×10^{-11}	3.2	3.1×10^{-16}	2.6
	Ne+Pb	4.4×10^{-6}	4.1	1.3×10^{-11}	3.7	0.6×10^{-11}	3.9		
		5.6×10^{-6}	4.1	1.6×10^{-11}	3.7	1.6×10^{-11}	3.7	7.2×10^{-17}	3.1
800	C+C	3.0×10^{-5}	3.1	6.0×10^{-10}	2.8	6.0×10^{-10}	2.8		
		1.3×10^{-5}	3.1	1.0×10^{-10}	2.7	1.0×10^{-10}	2.7	2.2×10^{-15}	2.1
	C+Pb	6.0×10^{-6}	3.9	2.5×10^{-11}	3.5	1.5×10^{-11}	3.5		
		6.1×10^{-6}	4.0	1.9×10^{-11}	3.6	1.9×10^{-11}	3.6	9.7×10^{-17}	3.0
800	Ne+NaF	1.6×10^{-5}	3.3	2.1×10^{-10}	2.8	1.6×10^{-10}	3.0		
		1.0×10^{-5}	3.3	0.6×10^{-10}	2.9	0.6×10^{-10}	2.9	9.3×10^{-16}	2.3
	Ne+Cu	8.0×10^{-6}	3.7	5.0×10^{-11}	3.2	4.0×10^{-11}	3.3		
		8.1×10^{-6}	3.6	3.6×10^{-11}	3.2	3.6×10^{-11}	3.2	3.1×10^{-16}	2.6
	Ne+Pb	4.0×10^{-6}	4.2	1.2×10^{-11}	3.7	0.6×10^{-11}	3.9		
		5.6×10^{-6}	4.1	1.6×10^{-11}	3.7	1.6×10^{-11}	3.7	7.2×10^{-17}	3.1
800	Ar+KCl	8.0×10^{-6}	3.5	3.5×10^{-11}	3.2	3.5×10^{-11}	3.2	3.0×10^{-16}	2.8
		8.0×10^{-6}	3.6	3.5×10^{-11}	3.2	3.5×10^{-11}	3.2	3.0×10^{-16}	2.6
	Ar+Pb	3.0×10^{-6}	4.3	0.9×10^{-11}	3.6	0.5×10^{-11}	3.7	3.0×10^{-17}	3.0
		5.0×10^{-5}	4.2	1.2×10^{-11}	3.8	1.2×10^{-11}	3.8	4.4×10^{-17}	3.2
2100	Ne+NaF	1.4×10^{-5}	3.5	0.5×10^{-10}	3.6	0.5×10^{-10}	3.6		
		1.0×10^{-5}	3.3	0.6×10^{-10}	2.9	0.6×10^{-10}	2.9	9.3×10^{-16}	2.3
	Ne+Pb	4.0×10^{-6}	4.2	0.6×10^{-11}	4.2	0.3×10^{-11}	4.4		
		5.6×10^{-6}	4.1	1.6×10^{-11}	3.7	1.6×10^{-11}	3.7	7.2×10^{-17}	3.1

Table 5: Coalescence coefficients, C_A, and interaction radii, R, observed (first row in each box) and calculated (second row in each box). All observed values are taken from Table VIII of reference [18], although many values for ^{4}He are missing. Calculations of C_A and R use equations (28) and (29), respectively.

		^{2}H		^{3}H		^{3}He		^{4}He	
Kinetic Energy (MeV/n)	Reaction	C_A	R (fm)	C_A	R (fm)	C_A	R (fm)	C_A	R (fm)
800	p+C	0.8×10^{-4}	3.0	4.0×10^{-9}	2.7	2.0×10^{-9}	3.1		
		0.2×10^{-4}	2.8	0.2×10^{-9}	2.4	0.2×10^{-9}	2.4	9.3×10^{-15}	1.8
	p+NaF	5.0×10^{-5}	3.3	1.0×10^{-9}	3.2	1.0×10^{-9}	3.2		
		1.6×10^{-5}	2.9	0.2×10^{-9}	2.5	0.2×10^{-9}	2.5	5.4×10^{-15}	1.9
	p+KCl	3.0×10^{-5}	3.5	5.0×10^{-10}	3.2	2.0×10^{-10}	3.7		
		1.4×10^{-5}	3.0	1.2×10^{-10}	2.6	1.2×10^{-10}	2.6	2.9×10^{-15}	2.0
	p+Cu	2.0×10^{-5}	3.7	3.0×10^{-10}	3.2	1.0×10^{-10}	3.8		
		1.2×10^{-5}	3.2	0.8×10^{-10}	2.8	0.8×10^{-10}	2.8	1.5×10^{-15}	2.2
	p+Pb	1.0×10^{-5}	3.9	3.0×10^{-11}	4.0	3.0×10^{-11}	3.7		
		0.8×10^{-5}	3.7	3.3×10^{-11}	3.3	3.3×10^{-11}	3.3	2.6×10^{-16}	2.7
2100	p+C	1.0×10^{-4}	2.8	5.0×10^{-9}	2.6	3.0×10^{-9}	2.9		
		0.2×10^{-4}	2.8	0.2×10^{-9}	2.4	0.2×10^{-9}	2.4	9.3×10^{-15}	1.8
	p+NaF	6.0×10^{-5}	3.1	1.0×10^{-9}	3.2	1.0×10^{-9}	3.2		
		1.6×10^{-5}	2.9	0.2×10^{-9}	2.5	0.2×10^{-9}	2.5	5.4×10^{-15}	1.9
	p+KCl	3.0×10^{-5}	3.5	6.0×10^{-10}	3.1	2.0×10^{-10}	3.7		
		1.4×10^{-5}	3.0	1.2×10^{-10}	2.6	1.2×10^{-10}	2.6	2.9×10^{-15}	2.0
	p+Cu	2.0×10^{-5}	3.7	3.0×10^{-10}	3.2	1.0×10^{-10}	3.8		
		1.2×10^{-5}	3.2	0.8×10^{-10}	2.8	0.8×10^{-10}	2.8	1.5×10^{-15}	2.2
	p+Pb	1.0×10^{-5}	3.9	4.0×10^{-11}	3.8	2.0×10^{-11}	4.0		
		0.8×10^{-5}	3.7	3.3×10^{-11}	3.3	3.3×10^{-11}	3.3	2.6×10^{-16}	2.7

Table 5 continued.

	^{2}H	^{3}H	^{3}He	^{4}He
a (fm)	0.24	0.24	0.24	0.24
b (fm)	2.0	1.6	1.6	1.0

Table 6: Constants [18] used for calculation of the interaction radius given in equation (29).

	^{2}H	^{3}H	^{3}He	^{4}He
c_A	1.6×10^{-3}	6.9×10^{-7}	6.9×10^{-7}	1.3×10^{-10}

Table 7: Constant c_A determined from equation (30), and used for calculation of the coalescence coefficient, C_A, given in equation (28).

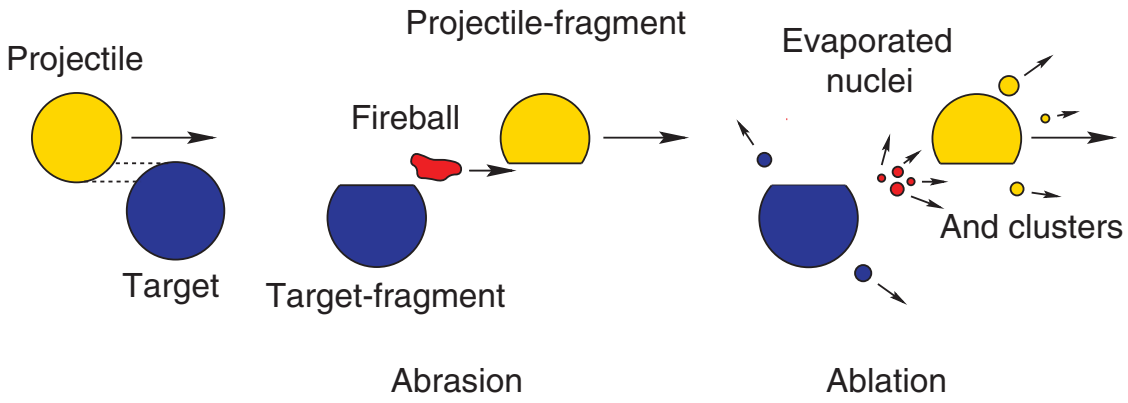

Figure 1: Formation of the central fireball region within the abrasion-ablation model. Figure reprinted from reference [16].

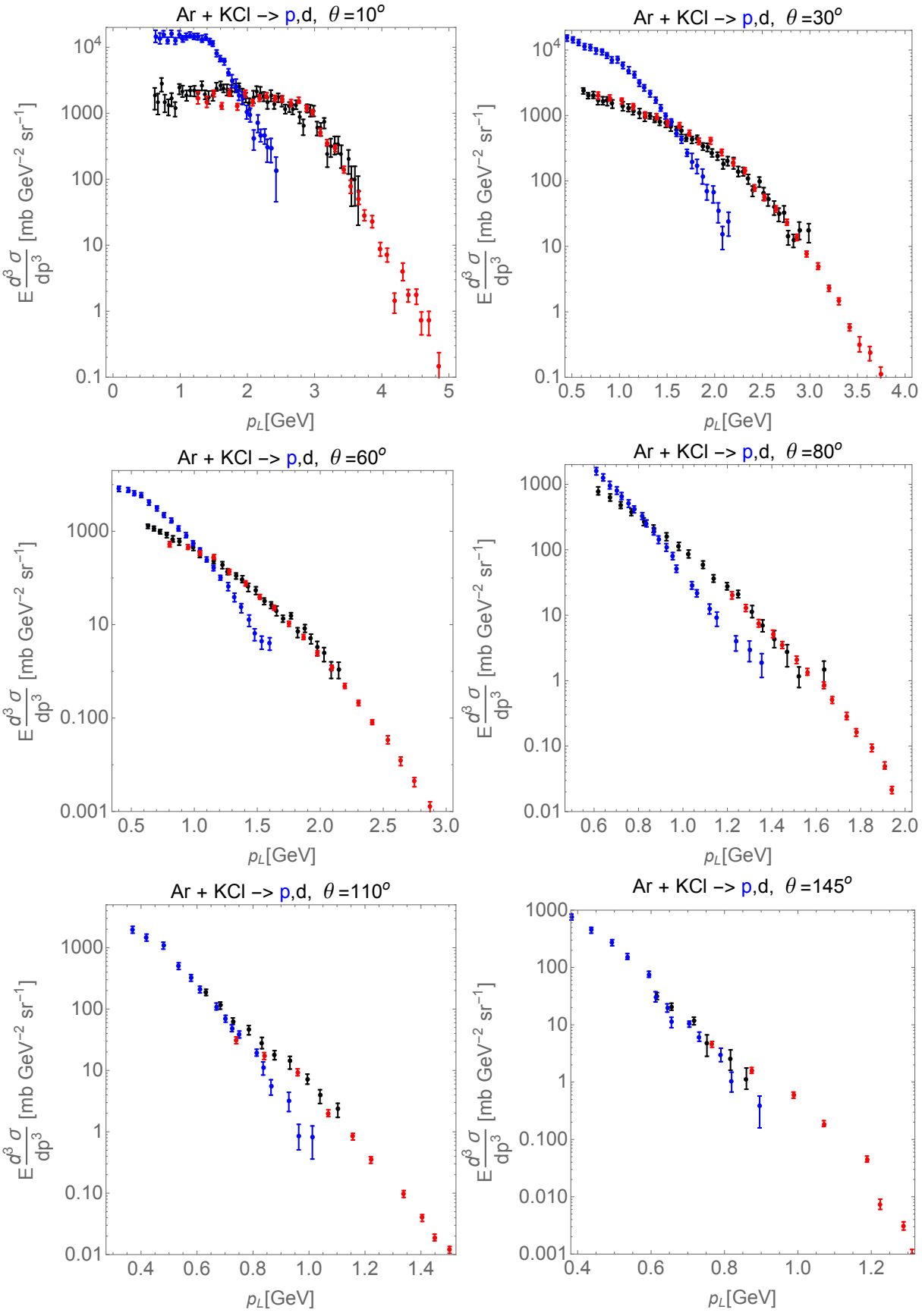

Figure 2: Deuteron (black) and proton production (blue) experimental [18] Lorentz-invariant double-differential cross sections as a function of lab momentum for Ar + KCl reactions at various production angles. The proton cross sections have been scaled (red) using the coalescence model of equation (4).

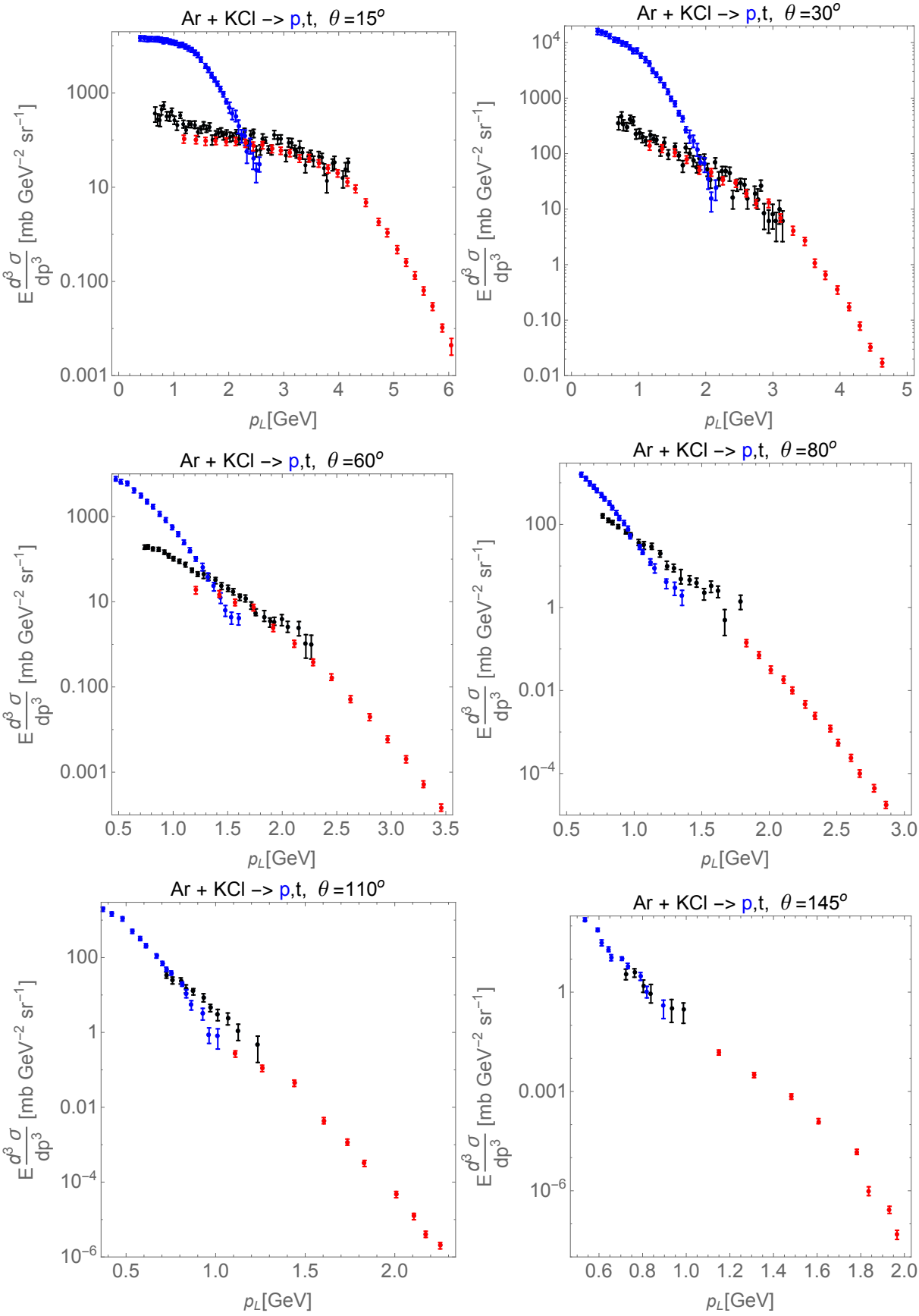

Figure 3: Triton (black) and proton production (blue) experimental [18] Lorentz-invariant double-differential cross sections as a function of lab momentum for Ar + KCl reactions at various production angles. The proton cross sections have been scaled (red) using the coalescence model of equation (4).

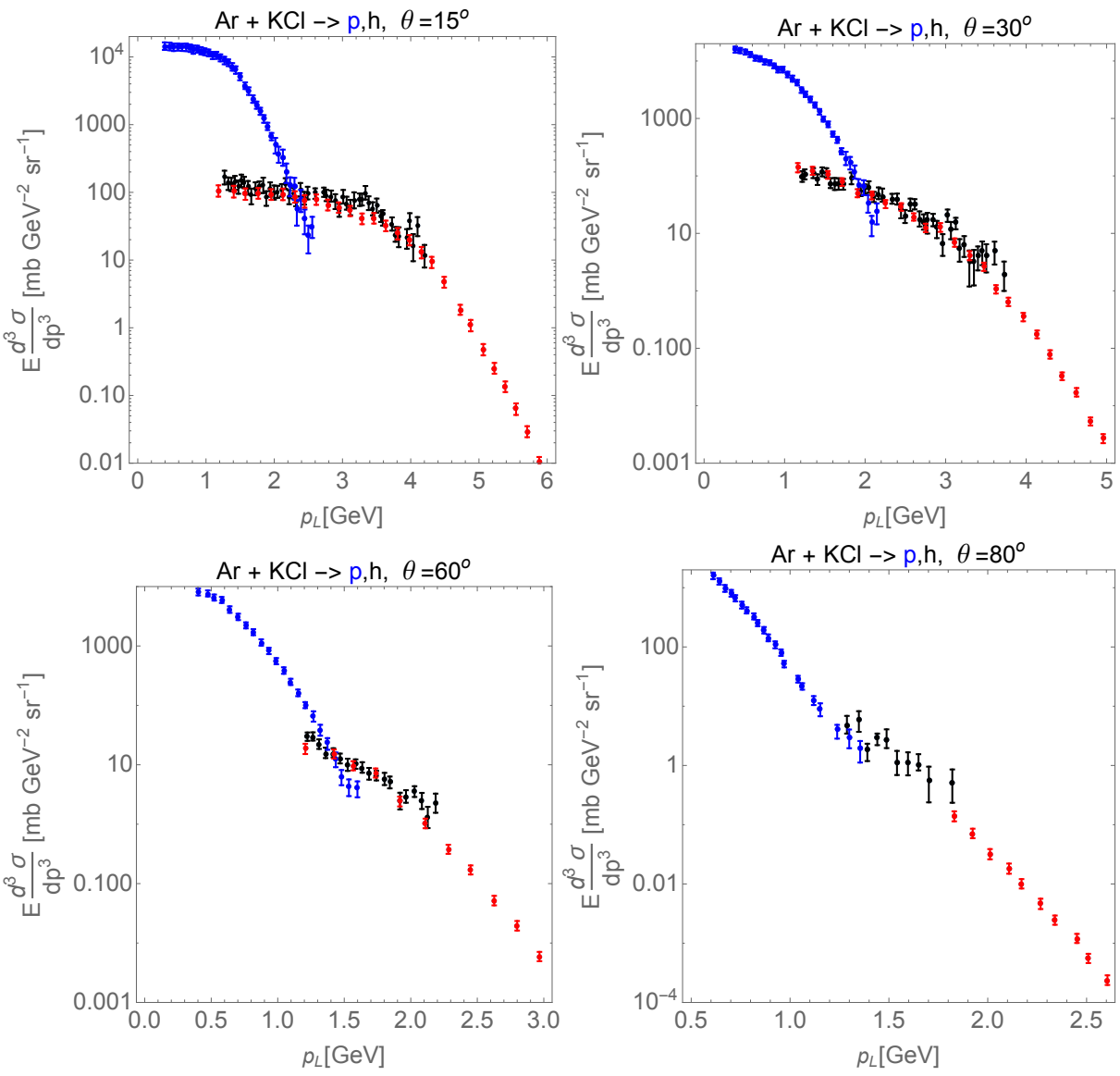

Figure 4: Helion (black) and proton production (blue) experimental [18] Lorentz-invariant double-differential cross sections as a function of lab momentum for Ar + KCl reactions at various production angles. The proton cross sections have been scaled (red) using the coalescence model of equation (4).

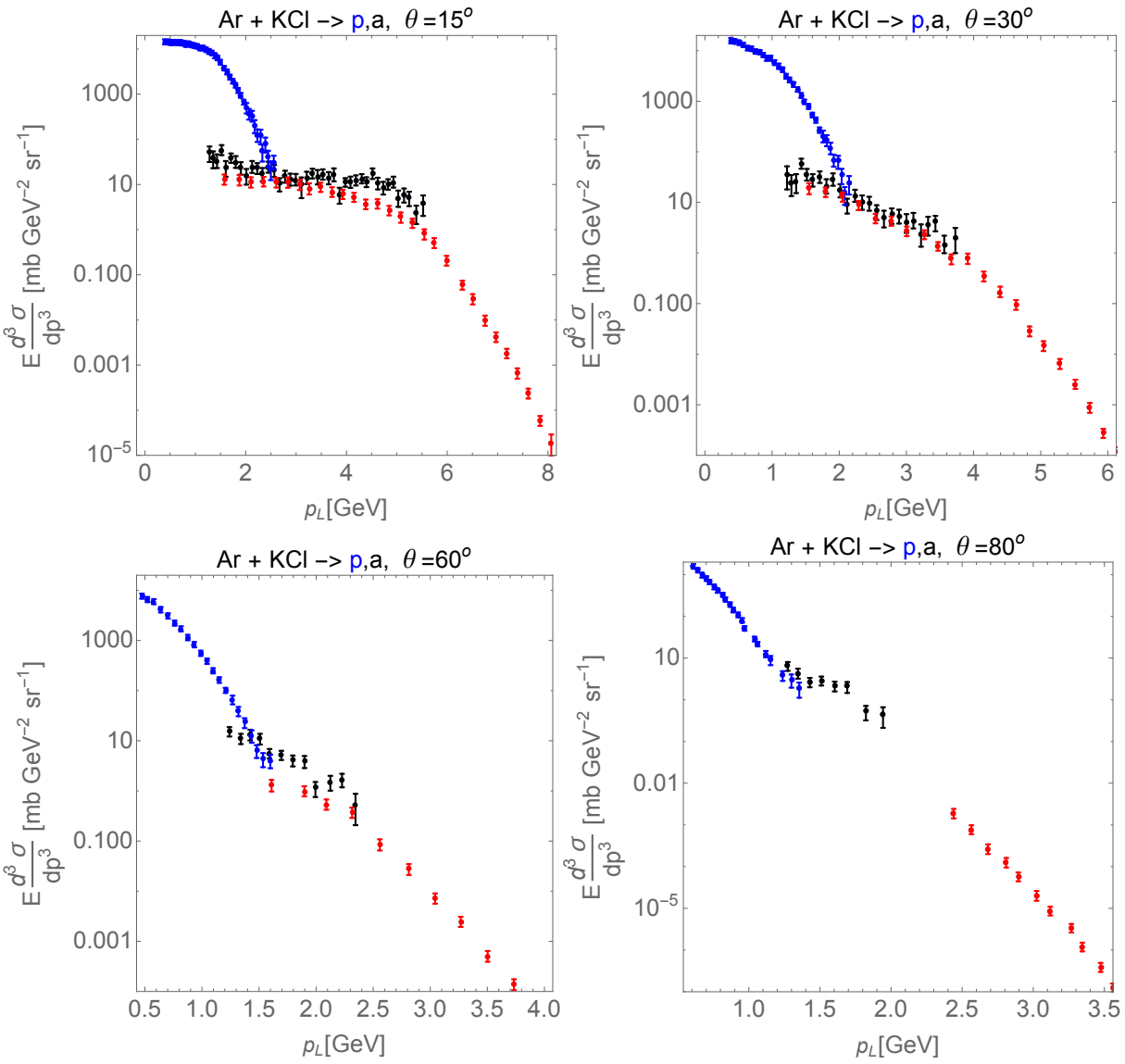

Figure 5: Alpha (black) and proton production (blue) experimental [18] Lorentz-invariant double-differential cross sections as a function of lab momentum for Ar + KCl reactions at various production angles. The proton cross sections have been scaled (red) using the coalescence model of equation (4).

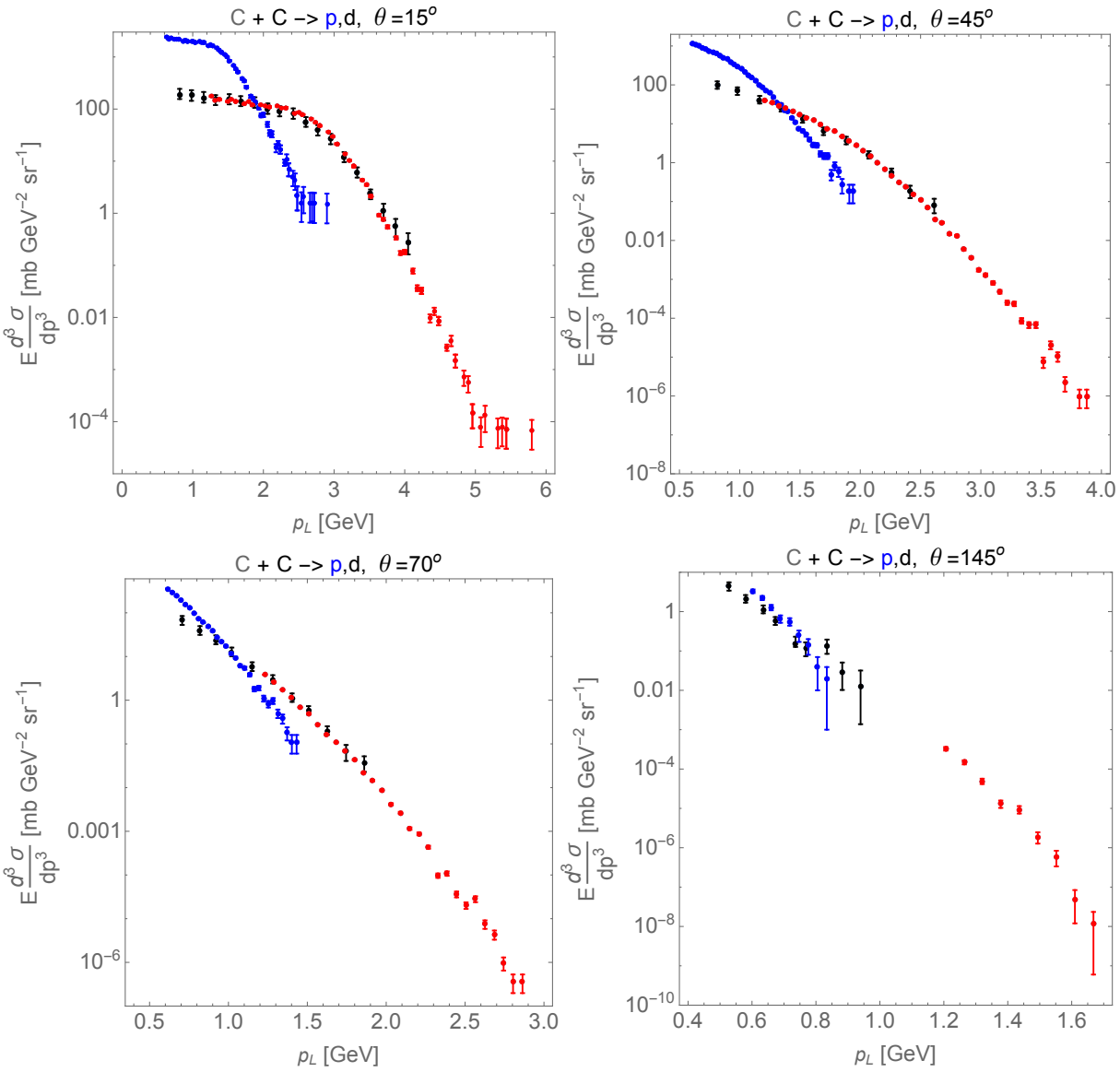

Figure 6: Deuteron (black) and proton production (blue) experimental [18, 29] Lorentz-invariant double-differential cross sections as a function of lab momentum for C + C reactions at various production angles. The proton cross sections have been scaled (red) using the coalescence model of equation (4).

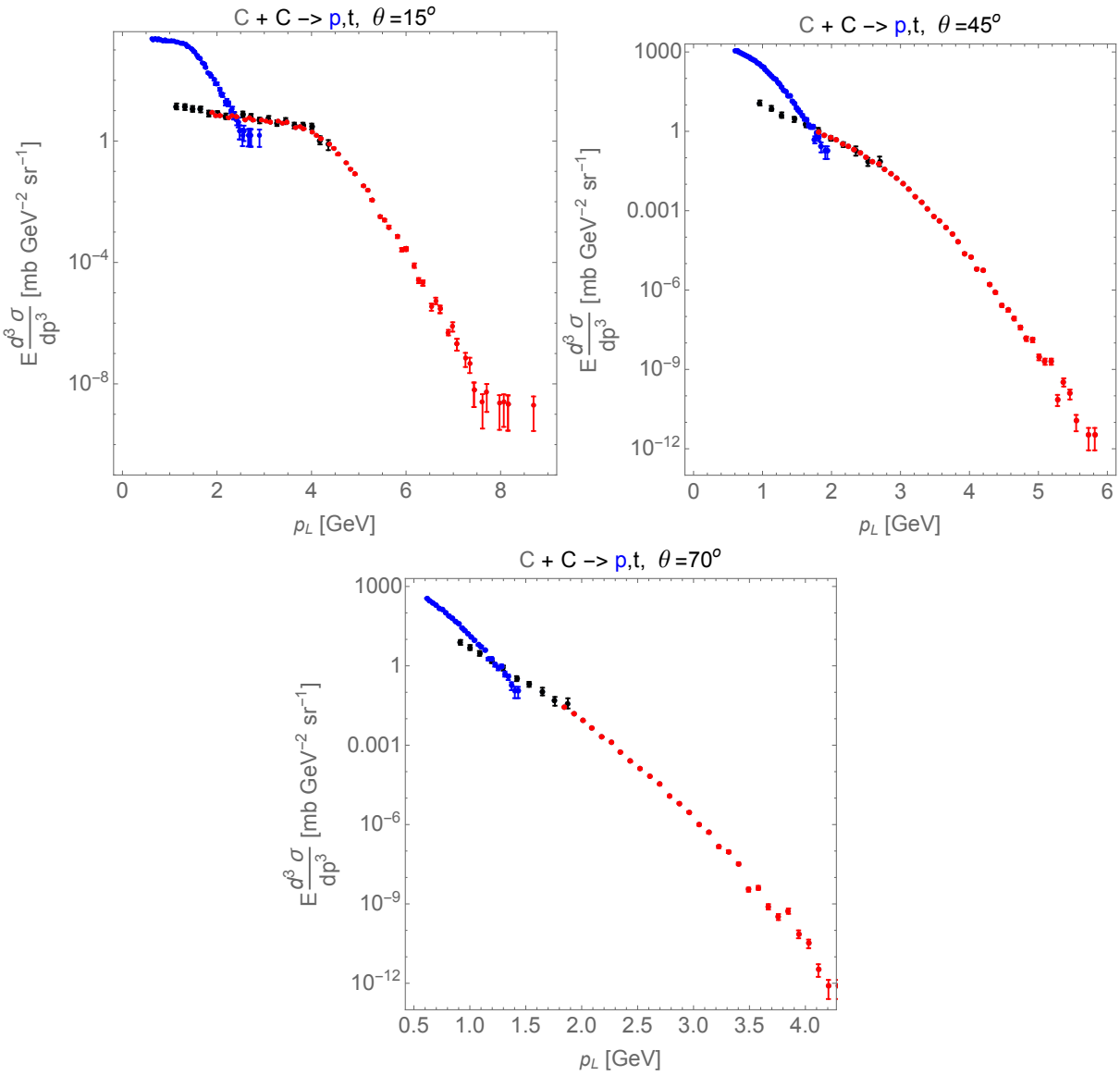

Figure 7: Triton (black) and proton production (blue) experimental [18, 29] Lorentz-invariant double-differential cross sections as a function of lab momentum for C + C reactions at various production angles. The proton cross sections have been scaled (red) using the coalescence model of equation (4).

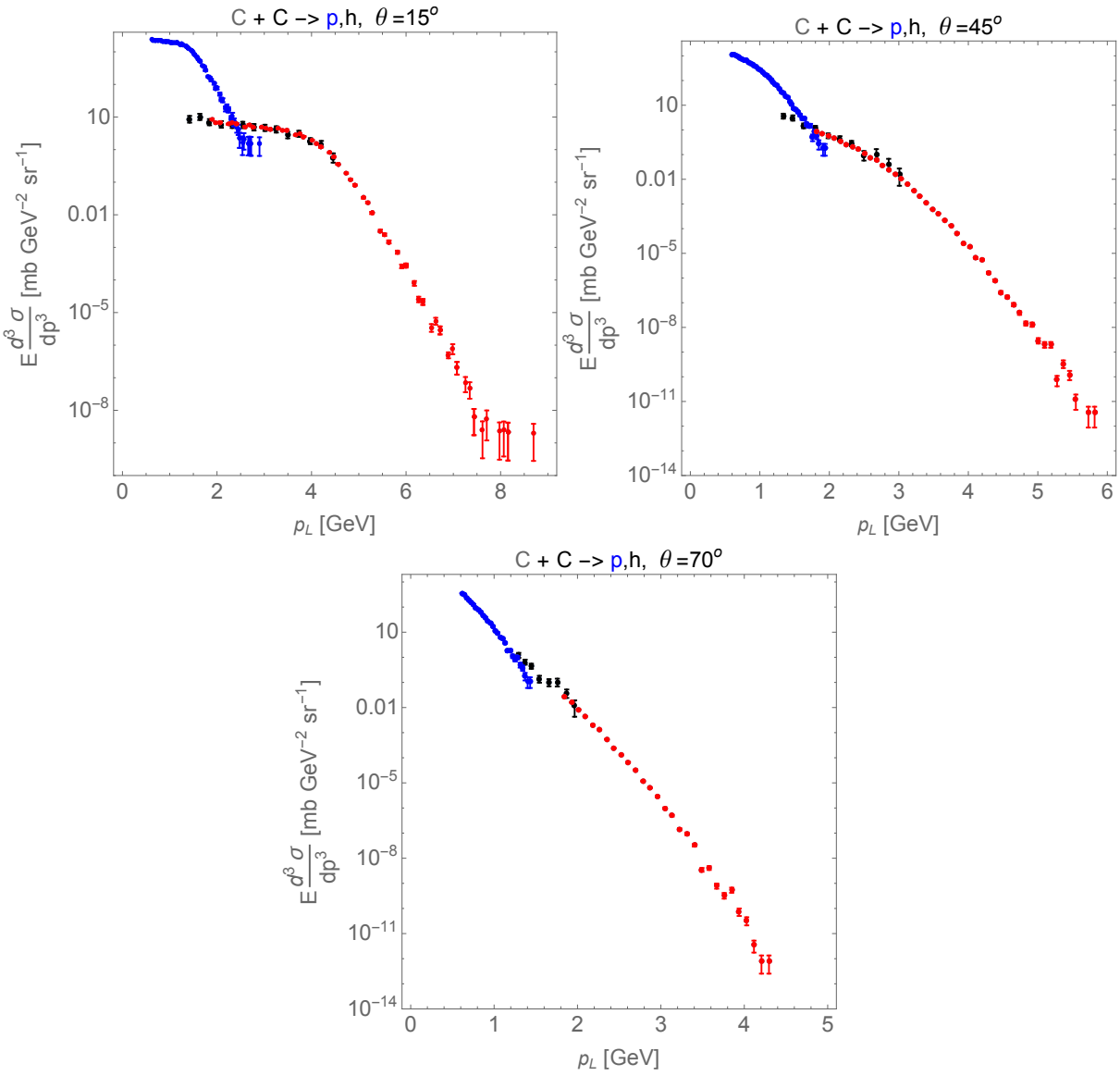

Figure 8: Helion (black) and proton production (blue) experimental [18, 29] Lorentz-invariant double-differential cross sections as a function of lab momentum for C + C reactions at various production angles. The proton cross sections have been scaled (red) using the coalescence model of equation (4).

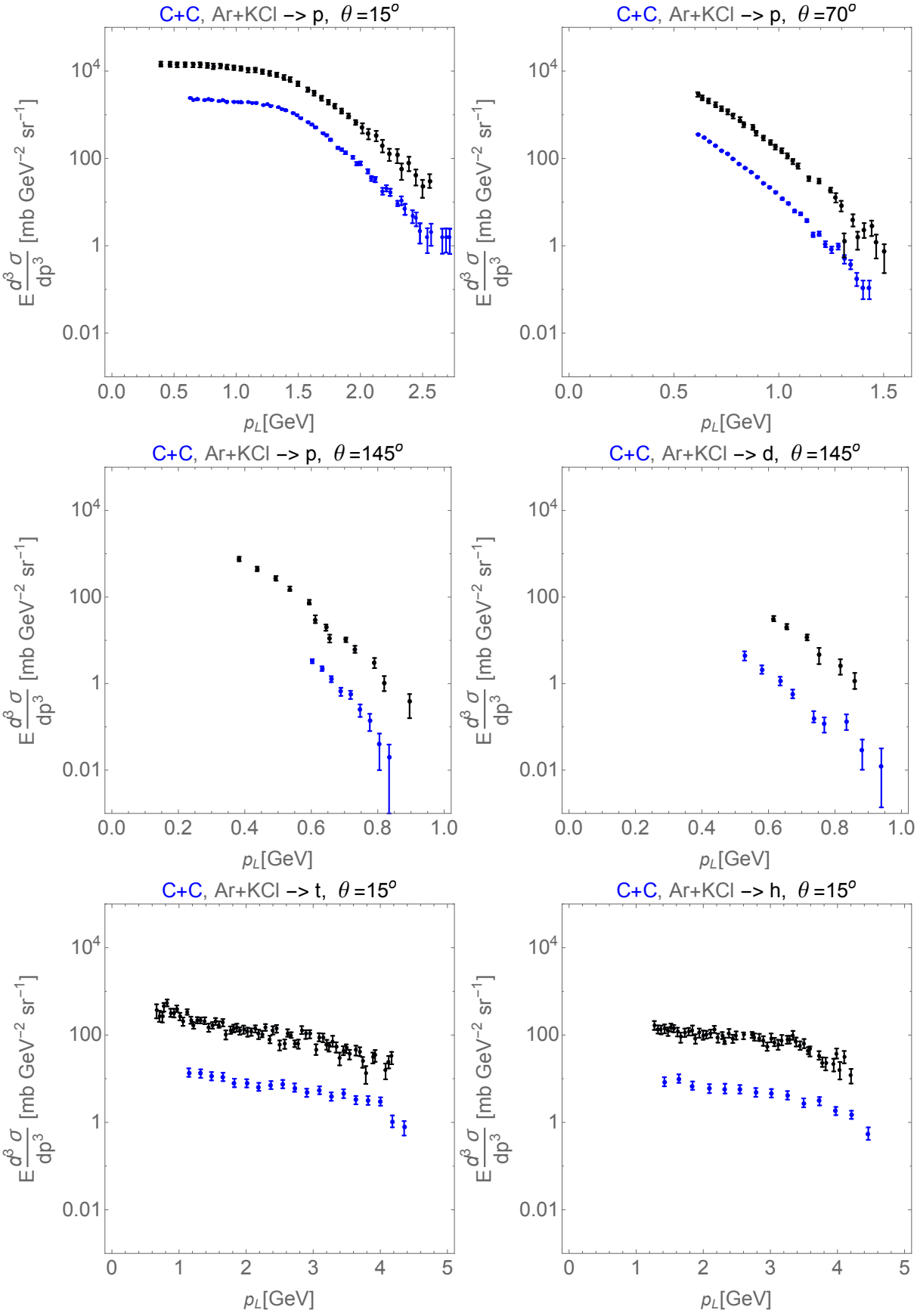

Figure 9: Proton, deuteron, triton and helion experimental data [18, 29] for Ar + KCl (black) and C + C (blue) reactions at various production angles, showing how the two sets of data compare to each other.

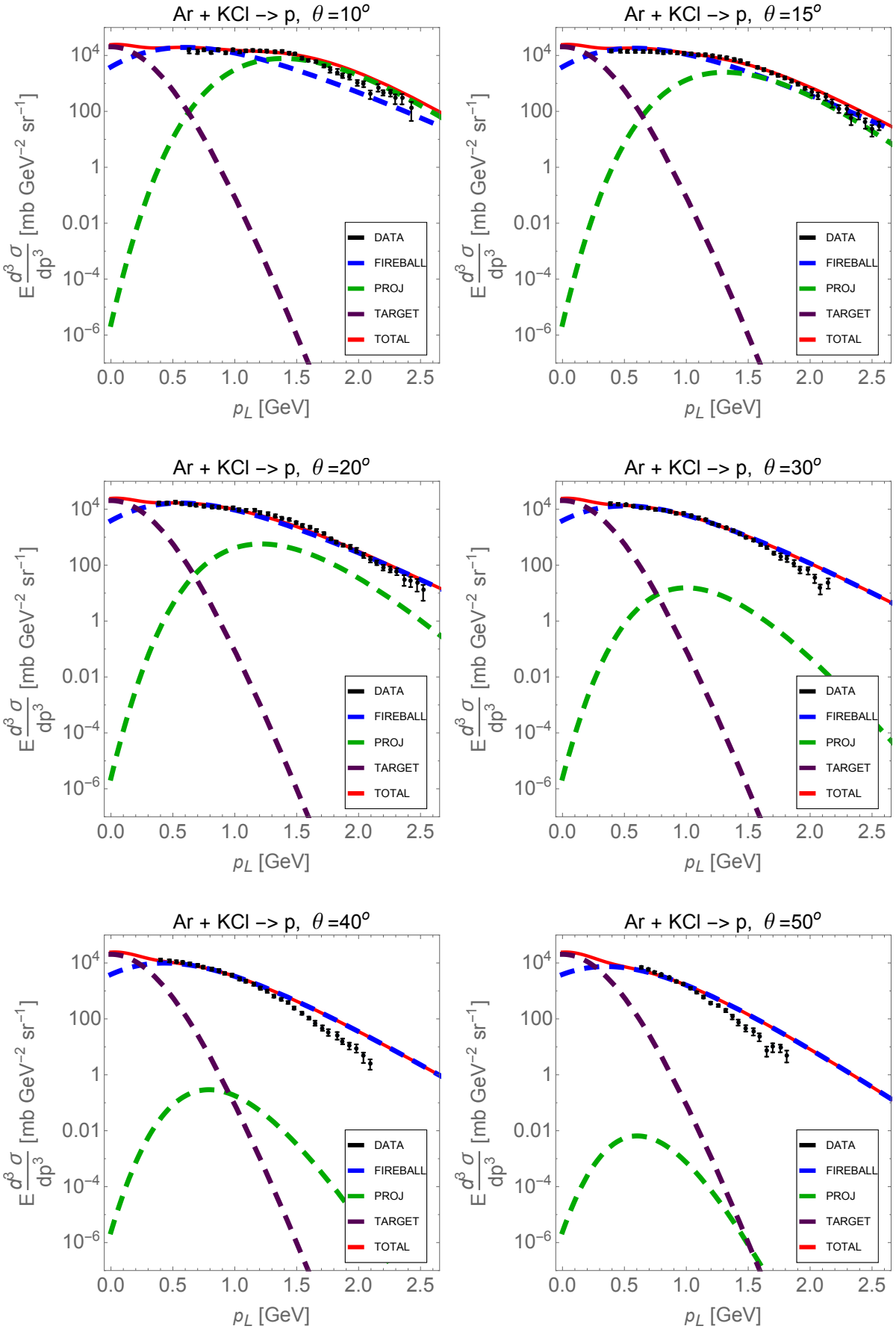

Figure 10: Proton thermal model cross sections at various production angles as a function of lab momentum for Ar + KCl reactions compared to experimental data [18]. Total (red) and individual contributions from projectile (green), target (purple) and central fireball (blue) are shown. (Figure is continued on the next page.)

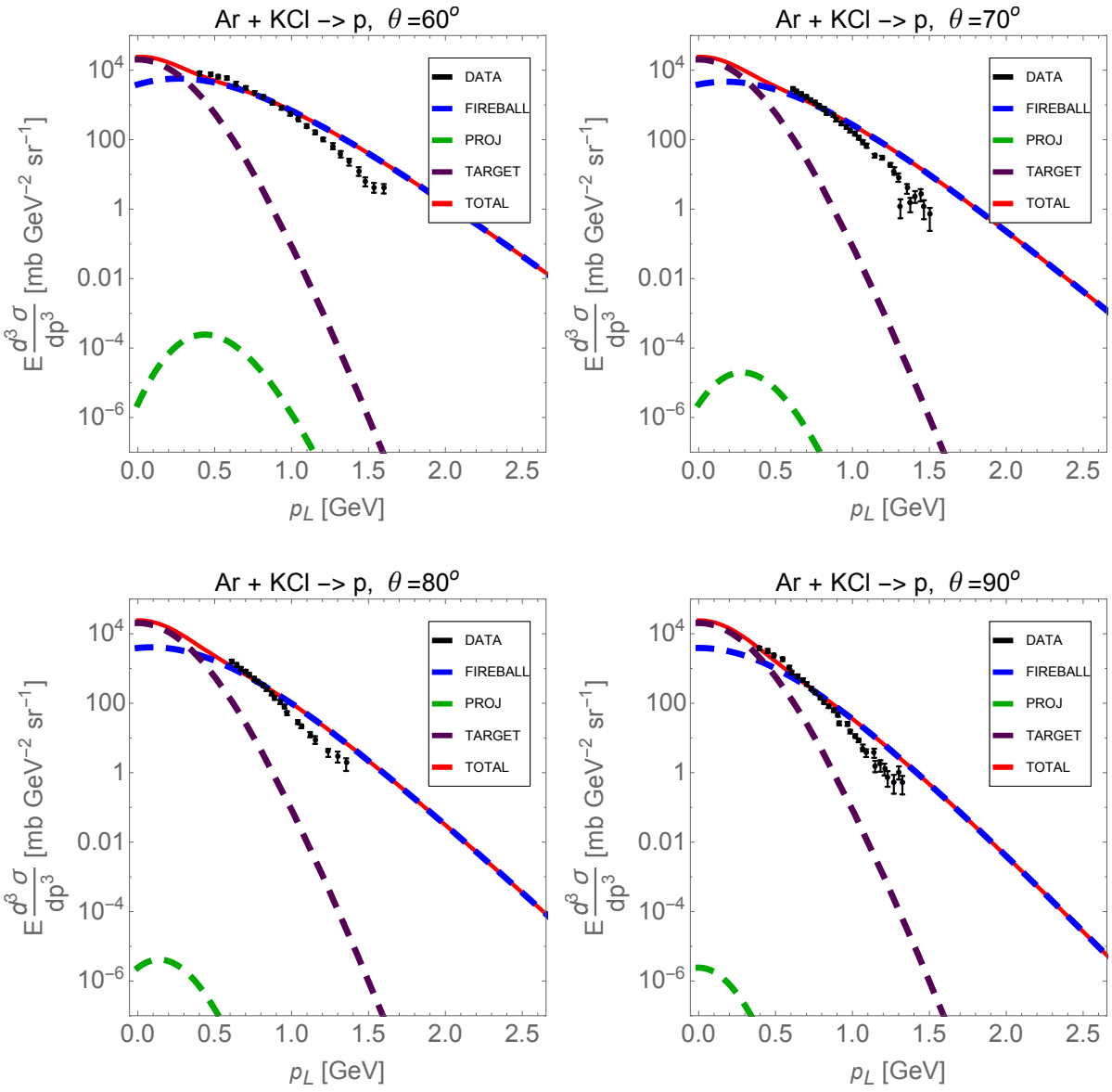

Figure 10 continued from previous page. Figure is also continued on the next page.

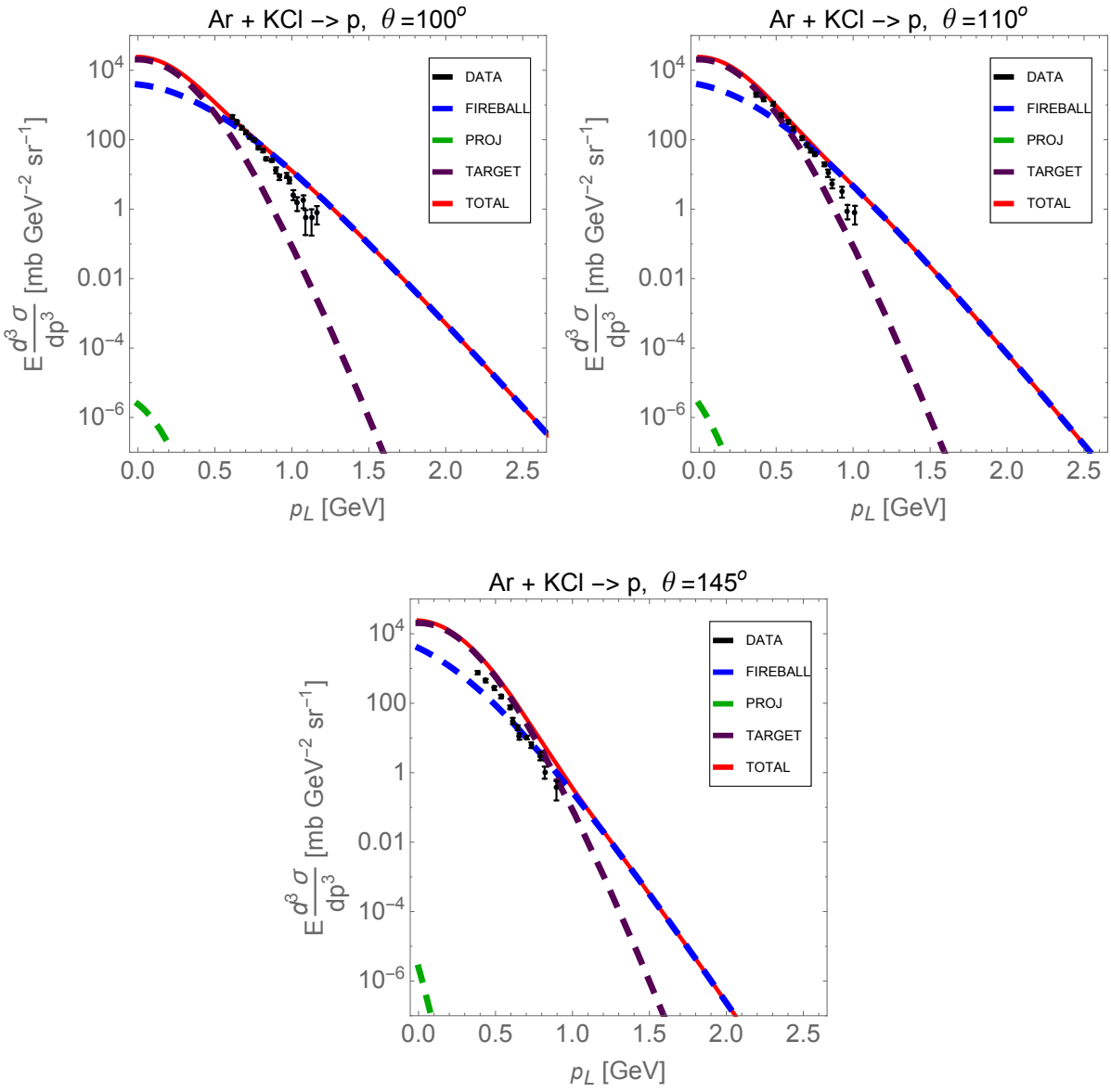

Figure 10 continued from previous page.

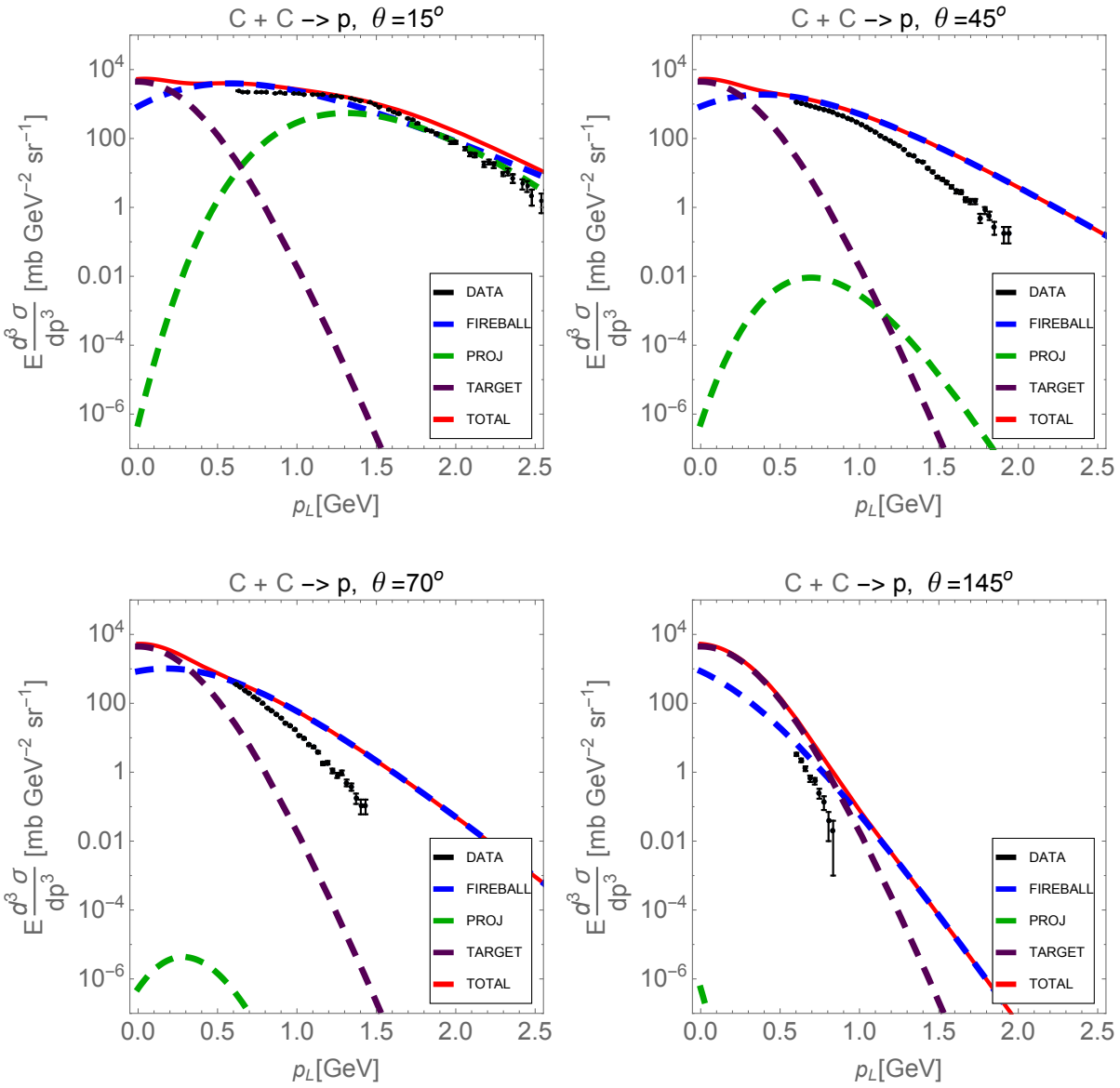

Figure 11: Proton thermal model cross sections at various production angles as a function of lab momentum for C + C reactions compared to experimental data [29]. Total (red) and individual contributions from projectile (green), target (purple) and central fireball (blue) are shown.

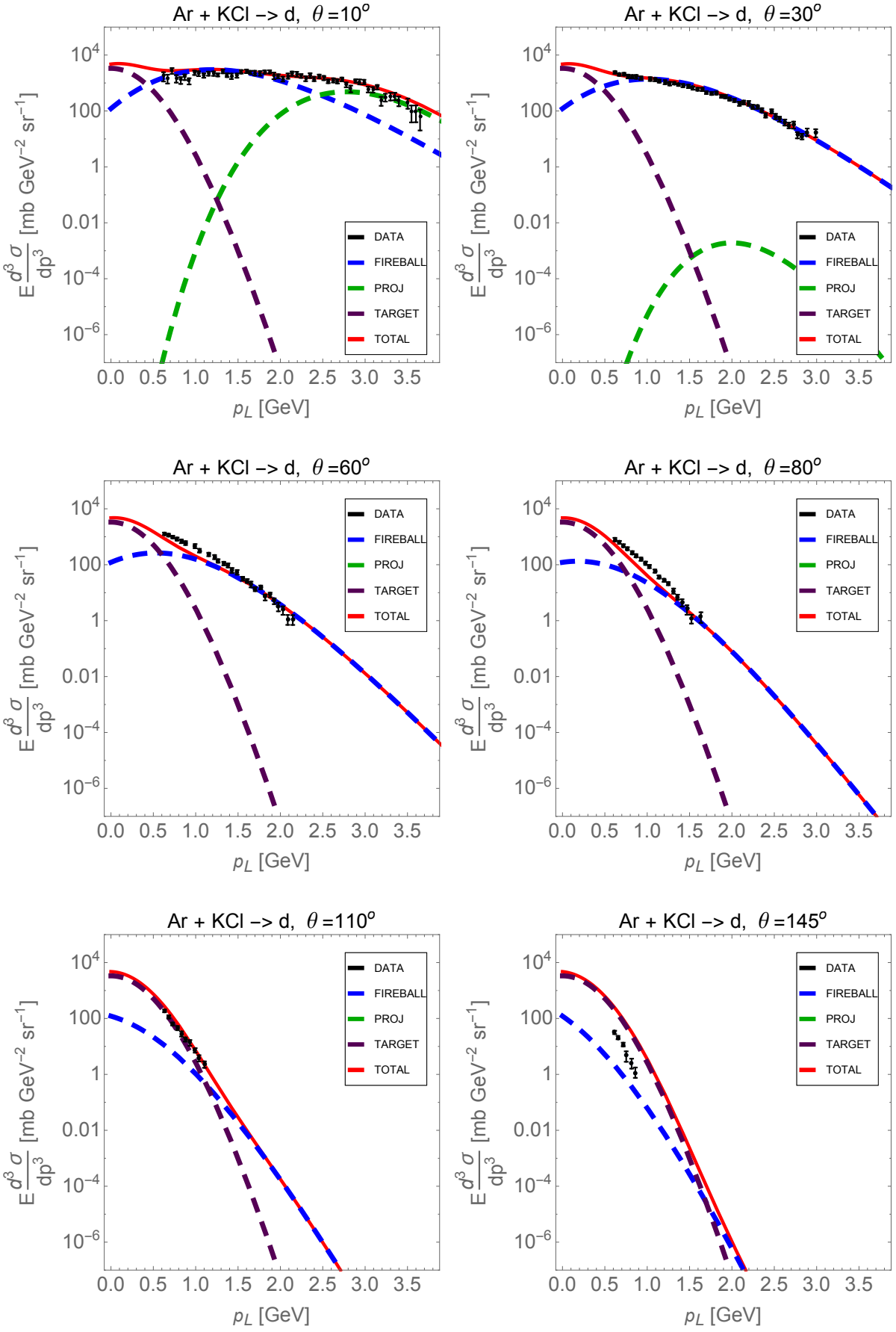

Figure 12: Deuteron coalescence model cross sections at various production angles as a function of lab momentum for Ar + KCl reactions compared to experimental data [18]. Total (red) and individual contributions from projectile (green), target (purple) and central fireball (blue) are shown.

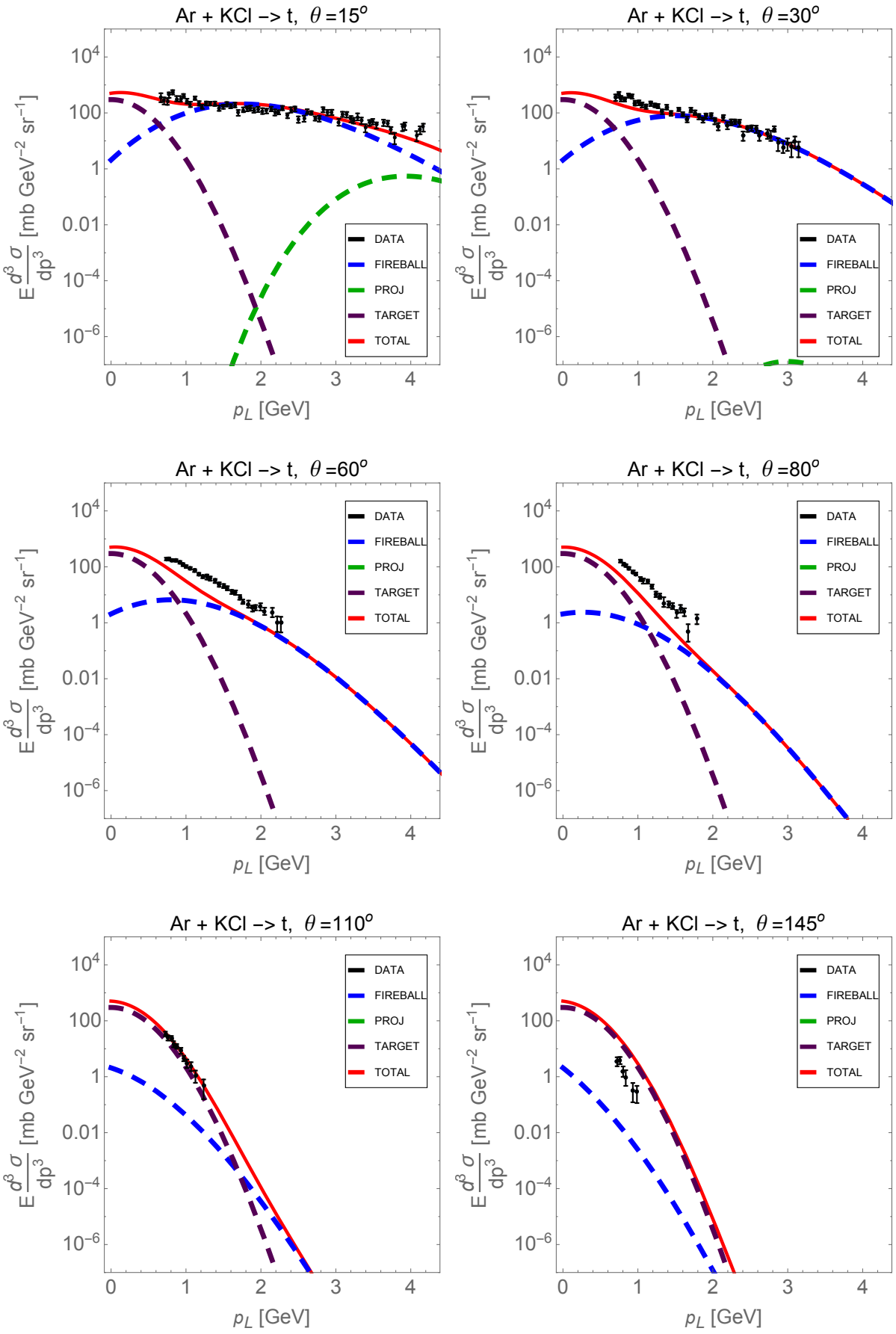

Figure 13: Triton coalescence model cross sections at various production angles as a function of lab momentum for Ar + KCl reactions compared to experimental data [18]. Total (red) and individual contributions from projectile (green), target (purple) and central fireball (blue) are shown.

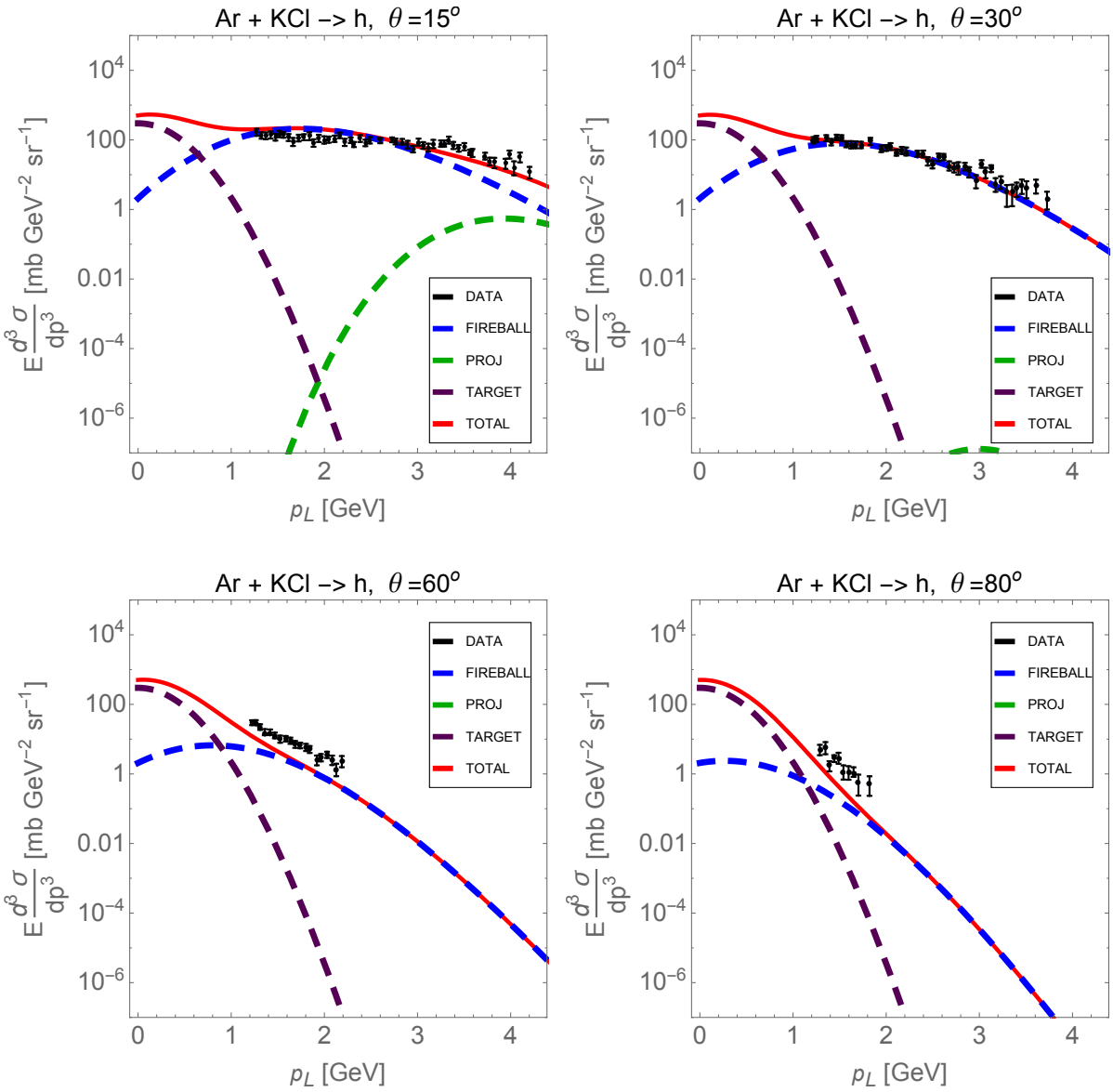

Figure 14: Helion coalescence model cross sections at various production angles as a function of lab momentum for Ar + KCl reactions compared to experimental data [18]. Total (red) and individual contributions from projectile (green), target (purple) and central fireball (blue) are shown.

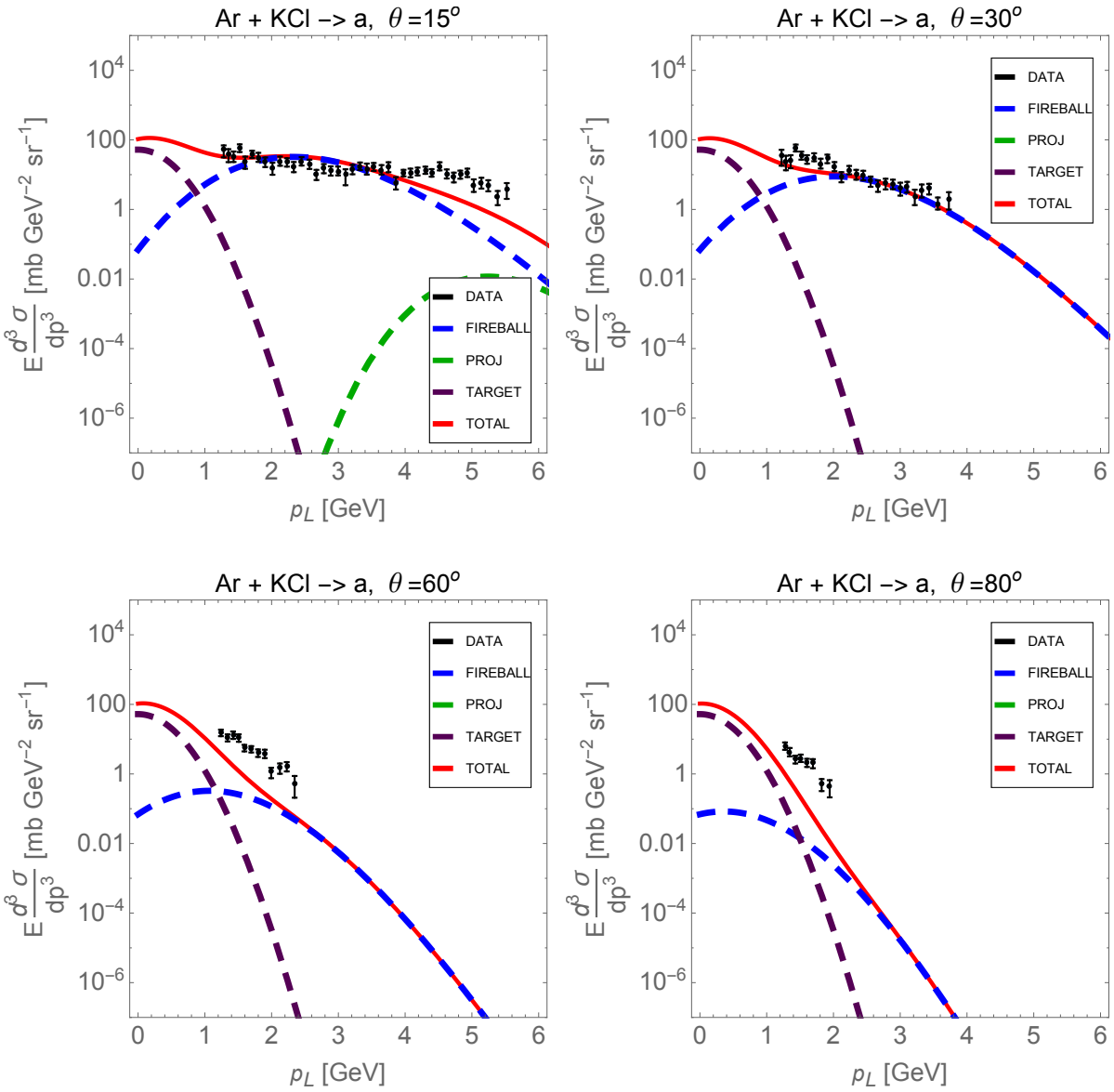

Figure 15: Alpha coalescence model cross sections at various production angles as a function of lab momentum for Ar + KCl reactions compared to experimental data [18]. Total (red) and individual contributions from projectile (green), target (purple) and central fireball (blue) are shown.

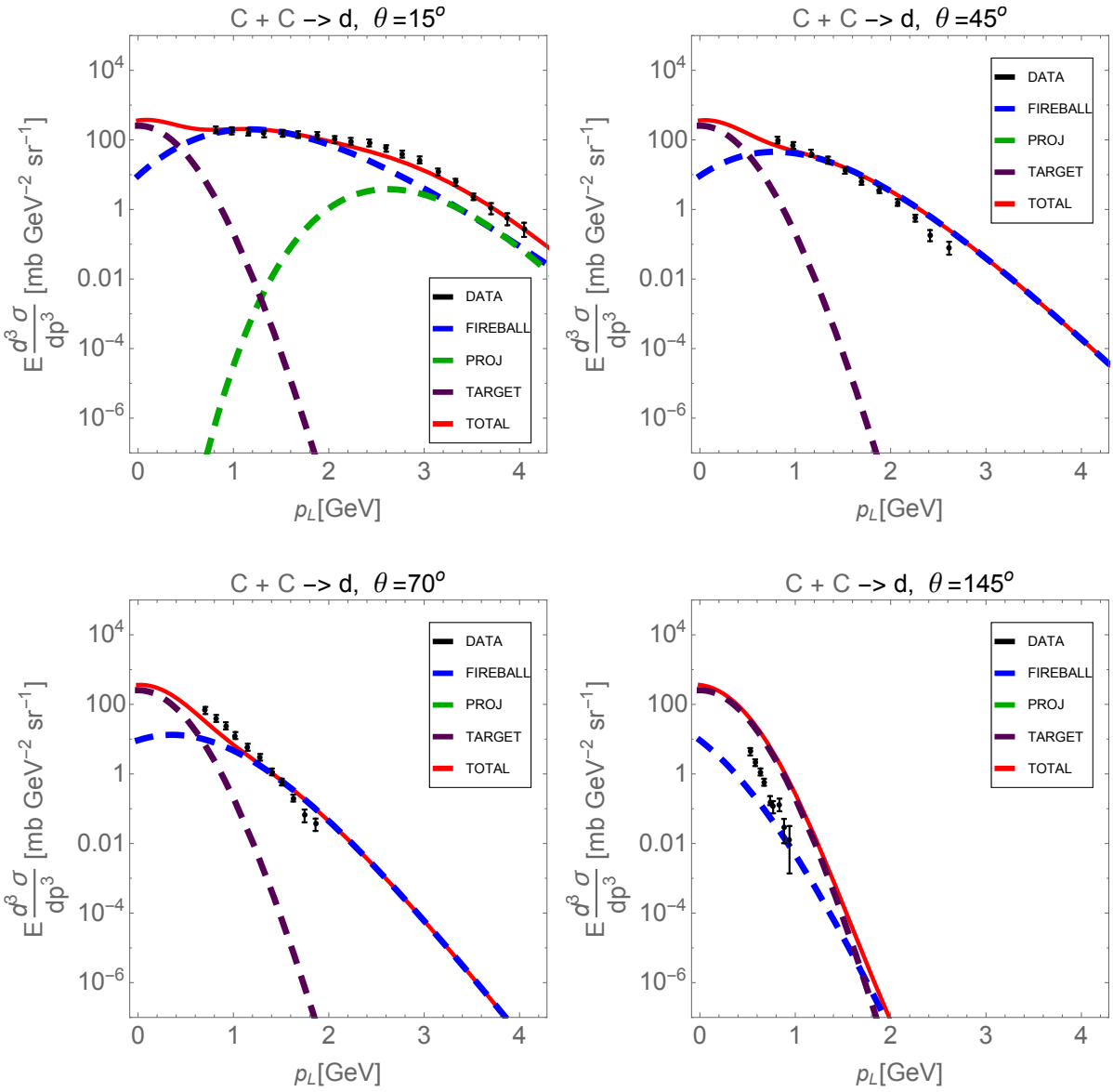

Figure 16: Deuteron coalescence model cross sections at various production angles as a function of lab momentum for C + C reactions compared to experimental data [18]. Total (red) and individual contributions from projectile (green), target (purple) and central fireball (blue) are shown.

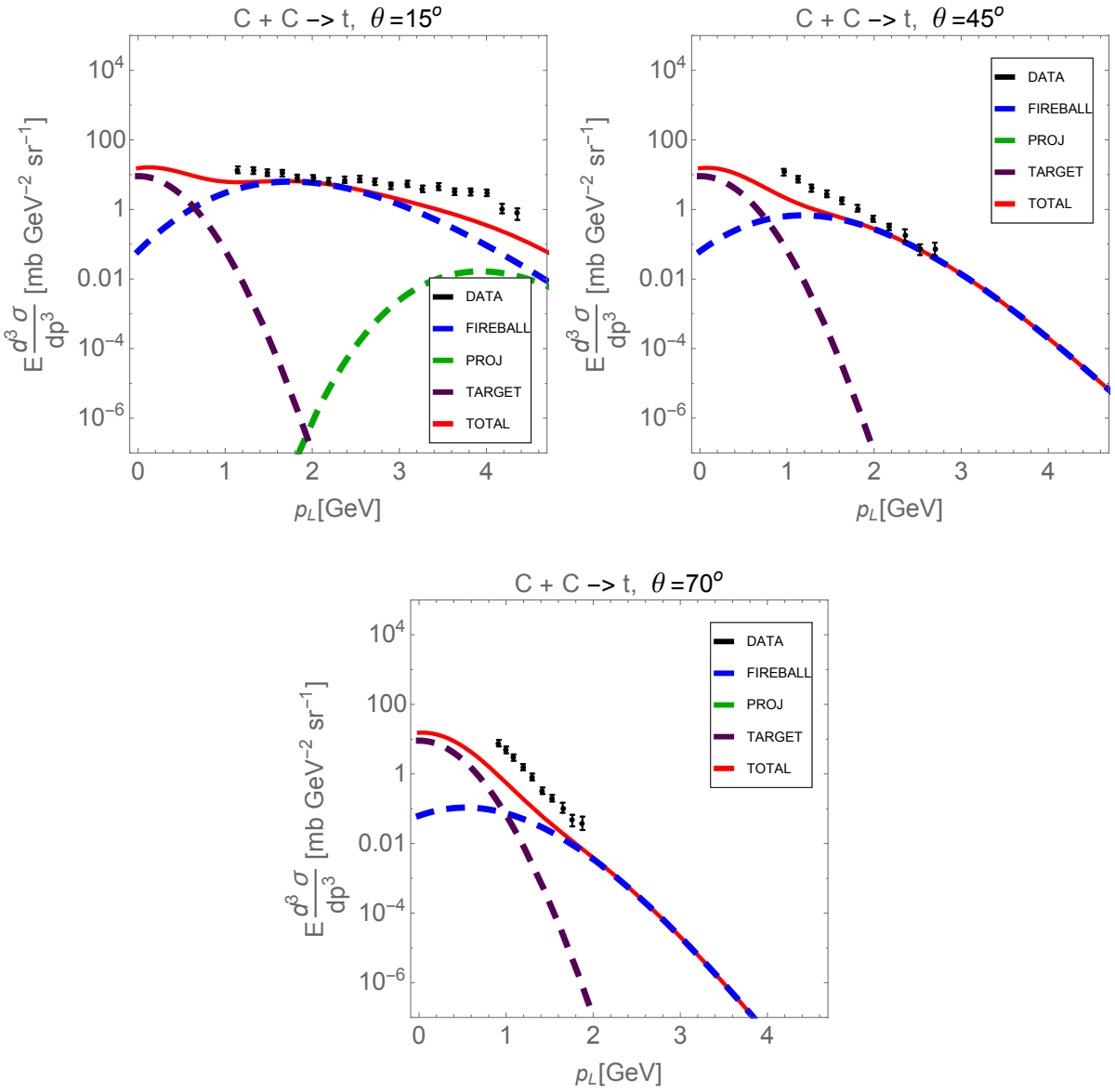

Figure 17: Triton coalescence model cross sections at various production angles as a function of lab momentum for C + C reactions compared to experimental data [18]. Total (red) and individual contributions from projectile (green), target (purple) and central fireball (blue) are shown.

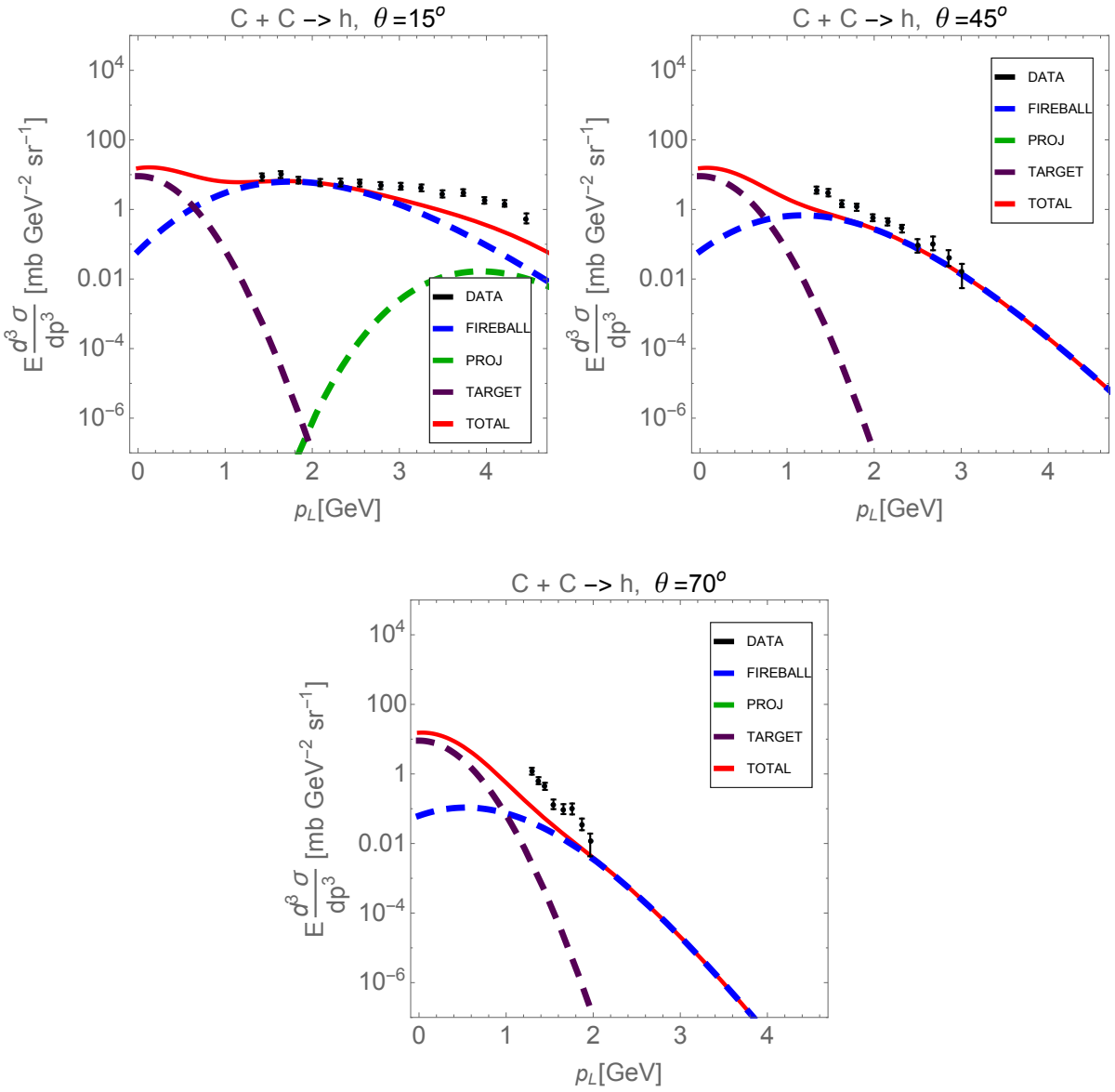

Figure 18: Helion coalescence model cross sections at various production angles as a function of lab momentum for C + C reactions compared to experimental data [18]. Total (red) and individual contributions from projectile (green), target (purple) and central fireball (blue) are shown.

References

[1] J.W. Norbury, T.C. Slaba, Life Sci. Space Res. 3 (2014) 90.

[2] Walker, S.A., L.W. Townsend, J.W. Norbury, Adv. Space Res. 51 (2013) 1792.

[3] J.W. Norbury, T.C. Slaba, N. Sobolevsky, B. Reddell, Life Sci. Space Res. 14 (2017) 64.

[4] J.W. Norbury, N., Sobolevsky, C.M. Werneth, Nucl. Instr. Meth. Phys. Res. B 418 (2018) 13.

[5] D. Matthia, et al., J. Space Weath. Space Clim. 6 (2016) A13.

[6] J.W. Wilson, L.W. Townsend, W. Schimmerling, G.S. Khandelwal, F. Khan, J.E. Nealy, F.A. Cucinotta, L.C. Simonsen, J.L. Shinn, J.W. Norbury, NASA Reference Publication 1257.

[7] J.W. Wilson, T.C. Slaba, F.F. Badavi, B.D. Reddell, A.A. Bahadori, Life Sci. Space Res. 2 (2014) 6.

[8] J.W. Wilson, T.C. Slaba, F.F. Badavi, B.D. Reddell, A.A. Bahadori, Life Sci. Space Res. 4 (2015) 46.

[9] J.W. Wilson, T.C. Slaba, F.F. Badavi, B.D. Reddell, A.A. Bahadori, Life Sci. Space Res. 7 (2015) 27.

[10] J.W. Wilson, T.C. Slaba, F.F. Badavi, B.D. Reddell, A.A. Bahadori, Life Sci. Space Res. 9 (2016) 69.

[11] T.C. Slaba, J.W. Wilson, F.F. Badavi, B.D. Reddell, A.A. Bahadori, Life Sci. Space Res. 9 (2016) 77.

[12] A.M. Adamczyk, R.B. Norman, S. Sriprisan, L.W. Townsend, J.W. Norbury, S.R. Blattnig, T.C. Slaba, Nucl. Instr. Meth. Phys. Res. A 678 (2012) 21.

[13] J.W. Norbury, J. Miller, A.M. Adamczyk, L.H. Heilbronn, L.W. Townsend, S.R. Blattnig, R.B. Norman, S.B. Guetersloh, C.J. Zeitlin, Rad. Meas. 47 (2012) 315.

[14] J.W. Norbury, J. Phys. Conf. Ser. 381 (2012) 012117.

[15] J.W. Norbury, J. Miller, Health Phys. 103 (2012) 640.

[16] M. Durante, F.A. Cucinotta, Rev. Mod. Phys. 83 (2011) 1245.

[17] R.L. Auble, Phys. Rev. C 28 (1983) 1552.

[18] S. Nagamiya, M.C. Lemaire, E. Moeller, S. Schnetzer, G. Shapiro, H. Steiner, I. Tanihata, Phys. Rev. C 24 (1981) 971.

[19] G.D. Westfall, J. Gossett, P.J. Johansen, A.M. Poskanzer, W.G. Meyer, H.H. Gutbrod, A. Sandoval, R. Stock, Phys. Rev. Lett. 37 (1976) 1202.

[20] J.W. Norbury, S.R. Blattnig, NASA Technical Publication 2008-215544.

[21] G. Israelian, Nature 489 (2012) 37.

[22] J.C. Howek, N. Lehner, B.D. Fields, G.J. Mathews, Nature 489 (2012) 121.

[23] A.M. Mukhamedzhanov, Shubhchintak, C.A. Bertulani, Phys. Rev. C 93 (2016) 045805.

[24] M. Barbagallo et al., Phys. Rev. Lett. 117 (2016) 152701.

[25] A. Goudelis, M. Pospelov, J. Pradler, Phys. Rev. Lett. 116 (2016) 211303.

[26] A. Frebel, T.C. Beers, Physics Today, January (2018) 30.

[27] E. Pian, et al., Nature 551 (2017) 67.

[28] I. Bartos, Physics World 31 (2018) 23.

[29] M.C. Lemaire, S. Nagamiya, O. Chamberlain, G. Shapiro, S. Schnetzer, H. Steiner, I. Tanihata, Lawrence Berkeley Laboratory report number LBL-8463, 1978.

[30] J.W. Norbury, F. Dick, NASA Technical Publication 2008-215543.

[31] M.R. Spiegel, Mathematical Handbook, Schaum's Outline Series, McGraw-Hill, New York, p. 141, 1968.

[32] J.W. Norbury, A.M. Adamczyk, Nucl. Instr. Meth. Phys. Res. B 254 (2007) 177.

[33] J.W. Norbury, Nucl. Instr. Meth. Phys. Res. A 703 (2013) 220.

[34] J.W. Norbury, Phys. Rev. C 79 (2009) 037901.

[35] C.M. Werneth, J.W. Norbury, S.R. Blattnig, Nucl. Instr. Meth. Phys. Res. B 298 (2013) 86.

[36] D.M. Hassler, J.W. Norbury, G. Reitz, Life Sci. Space Res. 14 (2017) 1.

[37] D. Matthia, et al., Life Sci. Space Res. 14 (2017) 18.

[38] S.R. Blattnig, S.R. Swaminthan, A.T. Kruger, M. Ngom, J.W. Norbury, Phys. Rev. D 62 (2000) 094030.

[39] J.W. Norbury, L.W. Townsend, Phys. Rev. D 75 (2007) 034001.

[40] L. Anderson, W. Bruckner, E. Moeller, S. Nagamiya, S. Nissen-Meyer, L. Schroeder, G. Shapiro, H. Steiner, Phys. Rev. C 28 (1983) 1224.

[41] J. Banaigs, et al., Phys. Rev. C 35 (1987) 1416.

[42] J. Gossett, H.H. Gutbrod, W.G. Meyer, A.M. Poskanzer, A. Sandoval, R. Stock, G.D. Westfall, Phys. Rev. C 16 (1977) 629.

[43] J. Papp, Lawrence Berkeley Laboratory report number LBL-3633. 1975.

[44] J.W. Norbury, Pion production in relativistic heavy ion collisions. Ph.D. dissertation, University of Idaho, 1983.

[45] F.H. Liu, Chinese J. Phys. 42 (2004) 694.

[46] J. Gossett, J.I. Kapusta, G.D. Westfall, Phys. Rev. C 18 (1978) 844.

[47] A.S. Goldhaber, H.H Heckman, Ann. Rev. Nucl. Part. Sci. 28 (1978) 161.

REPORT DOCUMENTATION PAGE

Form Approved
OMB No. 0704-0188

1. REPORT DATE *(DD-MM-YYYY)*	2. REPORT TYPE	3. DATES COVERED *(From - To)*
1-07-2018	Technical Publication	

4. TITLE AND SUBTITLE

Light Ion Double-Differential Cross Sections for Space Radiation

5a. CONTRACT NUMBER

5b. GRANT NUMBER

5c. PROGRAM ELEMENT NUMBER

6. AUTHOR(S)

Norbury, John W.

5d. PROJECT NUMBER

5e. TASK NUMBER

5f. WORK UNIT NUMBER

089407.01.23

7. PERFORMING ORGANIZATION NAME(S) AND ADDRESS(ES)

NASA Langley Research Center
Hampton, VA 23681-2199

8. PERFORMING ORGANIZATION REPORT NUMBER

L-20937

9. SPONSORING/MONITORING AGENCY NAME(S) AND ADDRESS(ES)

National Aeronautics and Space Administration
Washington, DC 20546-0001

10. SPONSOR/MONITOR'S ACRONYM(S)

NASA

11. SPONSOR/MONITOR'S REPORT NUMBER(S)

NASA-TP-2018-220077

12. DISTRIBUTION/AVAILABILITY STATEMENT

Unclassified
Subject Category 93
Availability: NASA STI Program (757) 864-9658

13. SUPPLEMENTARY NOTES

14. ABSTRACT

Neutrons and light ions have been shown to make large contributions to space radiation dose equivalent for realistic shielding scenarios. However, there are considerable uncertainties in the calculation of light ion production. Efficient and accurate calculation of light ion double-differential cross sections are required for input into space radiation transport codes. A thermal proton cross section model is developed which includes proton production from the 3 sources of projectile, central fireball, and target. It is shown that this 3-source model is able to explain the low-momentum, small-angle shoulder seen in proton spectra. Using the coalescence model, the thermal proton model is used to calculate light ion double-differential cross sections for use in space radiation transport codes. The 3-source model is also seen to be essential to explain the light ion shoulders, which are even more pronounced than the proton shoulders. Extensive comparisons between models and experimental measurements are shown and necessary future work is discussed.

15. SUBJECT TERMS

Double-differential cross section; Light ion; Space radiation

16. SECURITY CLASSIFICATION OF:			17. LIMITATION OF ABSTRACT	18. NUMBER OF PAGES	19a. NAME OF RESPONSIBLE PERSON
a. REPORT	b. ABSTRACT	c. THIS PAGE			STI Help Desk (email: help@sti.nasa.gov)
U	U	U	UU	59	19b. TELEPHONE NUMBER *(Include area code)* (757) 864-9658